EUROPEAN ORGANIZATION FOR NUCLEAR RESEARCH

BEAMSCOPE

Physics considerations, implementation,
and results of tests

H. Schönauer

CoRR : pp 7
10

57

CONTENTS

1. GENERALITIES

1.1 Introduction

BEAMSCOPE[1] is an acronym describing the action of the device on the beam; it stands for "BEtatron AMplitude Scraping by Closed-Orbit PErturbation". The acronym itself illustrates rather well the aim of this instrument: to provide a quick display of the (almost) complete transverse status of a beam in a circular accelerator. The transverse status of a beam is (in principle) defined by its density distribution in the four-dimensional betatron phase space. Assuming rotational symmetry in horizontal and vertical two-dimensional subspaces (i.e. smear-out of all initial inhomogeneities), the complete description reduces to a two-dimensional distribution on the plane of the two transverse betatron amplitudes.

In most practical cases there is amply sufficient information in the two projections, the horizontal and the vertical betatron amplitude distribution, respectively. From either of these two distributions, the corresponding transverse emittance -- regardless of its definition -- can be quickly calculated and displayed. In the configuration as realized in the PSB, Beamscope provides an amplitude distribution plus the 95% emittance values (the common definition in the PS complex) in a few seconds. The complete two-dimensional distribution can be obtained by simultaneous use of Beamscope in one plane and the measurement targets in the complementary plane (see Section 8). At present, this measurement requires several minutes, since the target has to be advanced manually.

The principle of operation is illustrated in Fig. 1. Three dipoles (the number required to produce a *local* closed-orbit bump), excited synchronously with a half-sine-like current produced by three pulsed power supplies, move the closed orbit away from its unperturbed location towards an appropriately placed precision scraper, where the beam is eventually lost, the largest betatron amplitudes first. This loss takes place gradually, typically within about 1 ms. During this interval, five signals are being recorded by five fast sampling ADCs: the shunt voltages of the three dipoles, the beam current (as provided by the slow beam-current transformer), and its electronically produced derivative. These "raw" signals are immediately transmitted via Serial CAMAC to a NORD 10 computer -- at present the Temporary Beam Measurement Computer (T-BMC), in the future the PSB FEC within the new PS control system. Since the ADCs have 1K words of 10-bit resolution, the raw signals assume values between 1 and 1024. Figure 2 depicts the typical pattern of these five signals.

All the information necessary to compute the amplitude of the closed-orbit bump (at the azimuth of the precision scraper) from the three dipole shunt signals, is stored in the computer. This synthetic signal, the "computed bump amplitude",

together with the two remaining raw signals I_{beam} and dI_{beam}/dt normalized to 1, constitute the three basic Beamscope signals. Figure 3 shows them, and also shows how the 95% beam radius can be derived directly from these signals (for more details and information about how the calibrated amplitude profiles are computed, see Section 2).

Obviously, the measurement as sketched here is fully destructive. On the other hand, and contrary to the non-destructive beam profile detectors, it gives directly the betatron *amplitude* distribution, which is easy to interpret and shows many more details than the projected density (see Fig. 5). In order to obtain the amplitude distribution from a profile detector, one has to use the Abel-transform[2], even in order to compute only the simple 95% emittances. This adds further loss of resolution to the sometimes intrinsically poor resolution of the profile detector.

Furthermore, the unwanted beam destruction can be 90% avoided if only emittance is to be measured (see Section 2).

1.2 History

As the basic principle of Beamscope is rather simple -- just produce a controlled closed-orbit bump and observe ensuing beam loss -- it has certainly been used in one or the other accelerator for coarse measurement of transverse beam dimensions. The only publication I know about deals with application of the method in context with the LBL Electron Ring Accelerator[3].

Independently, Beamscope was proposed for the PS Booster by Peter W. Krempl. He demonstrated its feasibility for the PSB[4] (which, depending on machine lattice and geometry, is not guaranteed *a priori*), proposed the two measurement methods described in subsections 2.1.1 and 2.1.2, and already pointed out most of the possible sources of measurement errors. He proposed a computer-assisted (IBM 1800) facility, which at the time was not adopted for budgetary reasons -- this in spite of a keen show of interest, on the part of the machine experimenters, in replacing the IBS (Ionization Beam Scanner); this had been shown to be inadequate for emittance measurement of (highly) bunched beams[5] and had consequently been put out of operation. P. Krempl left CERN and F. Sacherer pursued the realization of the idea in a different way: deliberately renouncing computer assistance, he conceived a system that was only capable of giving the (95%) beam diameter by the double-pulse method (see subsection 2.1.2), the so-called "Beam Width Meter" (BWM). The bump amplitude was determined by a position monitor situated immediately upstream of the precision scraper. This system was actually built, and worked in principle, but the measured beam diameters differed substantially and unsystematically from the ones measured with targets. This failure was never fully explained but in the light of later experiments[6] it became probable that the accuracy of a pick-up electrode plus its complex electronics is not sufficient (in particular in the presence of beam loss) for this kind of application.

With the hardware of the BWM and using the DPO (Tektronix WP1000 Digital Processing Oscilloscope) to compute the bump amplitude from the shunt signals of the three dipoles, I was able to measure transverse beam dimensions in fair agreement with target values. Moreover, the errors behaved rather systematically and led to the idea that the measurement targets might have aged and that their results were erroneous. This conjecture has been confirmed in the meanwhile.

These experiments pointed out how to proceed further: back to the computed (from dipole currents) bump amplitude. Succeeding F. Sacherer in charge of the implementation of Beamscope, I had extensive computer studies done[7] to check the feasibility of the method with existing hardware, mainly with respect to parasitic scraping, the most insidious error source. It turned out that the configuration chosen from the very beginning was also the best, making Beamscope feasible for all working points, but nevertheless reducing the vertical acceptance of the PSB to about 90π mm·mrad. Precise measurements of all of the 24 ring dipoles[8] involved were done[9] in order to verify whether their field quality was appropriate for this application. Since the field quality of the dipoles was found to be surprisingly good, it was only necessary to invest in interfacing the hardware to the Beam Measurement Computer, then a PDP 11/45. On the initiative of Metzger[10] and with the help of Baribaud and his team[11], a serial CAMAC loop was installed, together with the hardware described in subsection 5.4. This configuration was retained and is still operating successfully with the T-BMC. The bumper supplies had to be improved and modified to satisfy operation performance standards. Software turned out to be more complex than was foreseen and required considerable development. Even now, with the feedback from operational experience, software still continues to evolve slowly.

2. PRINCIPLE

2.1 Emittance measurement

Emittance measurement basically means measurement of the beam dimensions, which have to be defined in one way or the other. The definition of emittance E adopted for the CPS complex is the area of that ellipse in betatron phase space that comprises 95% of all particles. For a given azimuth, there is a corresponding beam radius given by the well-known expression $x(95\%) = [(E/\pi)\beta_{CS}]^{\frac{1}{2}}$; β_{CS}, the Courant-Snyder beta function for the azimuth considered, is known from lattice calculations. Although perhaps not the most significant definition [it completely ignores the particle distribution for amplitudes < $x(95\%)$], it is well adapted to target measurements and acceptance considerations and has proved to be useful in practice.

There are basically two methods for determining $x(95\%)$ [$\equiv x(95)$] with Beamscope; both were indicated by Krempl.

2.1.1 The single-pulse method [in earlier references,
       also called the Closed-Orbit Reconstruction
       (COR) method]

Its principle is well illustrated in Fig. 3, showing the three basic Beamscope signals. Recording the instant of 95% crossing of the beam current I, one immediately finds the corresponding bump amplitude y(95). The same can in principle be done with the end of the losses which obviously mark the "loss" of the particles of zero amplitude and hence designate the beam centre. Looking at the raw profile dI/dt, one notes, however, that the "end" of the loss is smeared a bit by the influence of the momentum spread. (This effect and the "tangent fit" described below are discussed in subsection 3.2). In order to define the beam centre properly, a tangent is put on the slope of dI/dt, and its intersection with the abscissa yields the beam centre or, in other words, the closed orbit. Looking up the corresponding bump amplitude y_0, the wanted beam radius x(95) is obviously given by

$$x(95) = y_0 - y(95) .$$

With the known diameter 2a of the precision collimator, one finds the (otherwise unknown) amplitude x_{co} of the unperturbed closed orbit:

$$x_{co} = \pm(y_0 - a) .$$

The sign depends on the "polarity" (e.g. "in" or "out") of the bump.

Physically, this procedure means that one assumes constant phase-space density in the vicinity of the origin: in this case the amplitude distribution is proportional to the area element[*] $dA = 2\pi\ r\ dr$. This concept would fail in case of a genuine hollow beam (which we were not yet able to produce ...).

Performing two measurements with different dipole polarities, the sum of the two y_0's should be equal to the width of the aperture:

$$y_{0,1} + y_{0,2} = 2a .$$

This provides a simple check of the validity of the measurement and can be used to verify calibrations, energy, and Q-values.

The single-pulse method being fully destructive, there may be a reaction of the beam control system perturbed by particles lost on pick-ups or simply by too low an intensity at the end of the scraping. This reaction may interfere with a (horizontal) measurement.

The total loss of the beam may limit the application of the method to routine monitoring of beam properties in normal operation.

---

[*] r is the radius of polar representation in x, $\beta_{cs}x'$.

2.1.2 The double-pulse method [formerly referred to as the Beam Width Meter (BWM) Method]

This method largely avoids the drawbacks of the preceding method: if only the 95% dimensions of the beam are to be found, one can stop the bumper supplies, once 5% of the beam are lost, by a "stop pulse" generated by a kind of comparator. The stop pulse causes the remaining energy stored in the capacitor banks of the bumper supplies to be dumped into a crowbar. This technique allows for emittance measurements with little more than 5% loss (the bumper supplies stopped, the closed-orbit bump amplitude continues to increase until eddy currents in the vacuum chamber have decayed). Figure 4 shows the principle of this method, which is even simpler than the single-pulse one: if the amplitude x_{co} of the unperturbed closed orbit was known, $x(95)$ would be simply

$$x_1(95) = a - y_1(95) - x_{co} \; ,$$

index 1 standing for polarity 1. For the other polarity (inverted bump amplitude) the analogous equation is

$$x_2(95) = a - y_2(95) - x_{co} \; .$$

Adding both equations yields the very simple expression:

$$x(95) = \frac{x_1(95) + x_2(95)}{2} = a - \frac{1}{2}\left[y_1(95) + y_2(95)\right]$$

which can also be read directly from Fig. 4.

One measurement necessitates two pulses and gives the beam dimensions averaged over the two shots (note that a series of n measurements only requires n+1 shots). It is this method that is used for operational emittance measurement.

2.2 Display of betatron amplitude distributions

From the raw signals of Fig. 3 it is straightforward to compute a calibrated curve representing the distribution of betatron amplitudes $dN/dx = n(x)$ ($\int n(x) \, dx = N$) or derived quantities as emittance variables. The computed bump amplitude $y(t)$ and the raw profile

$$-\frac{dI}{dt} = \frac{\beta}{C_1} \frac{dN}{dt}(t)$$

form a parameter representation of $(dN/dt)(x)$. $\left[C_1 = (2\pi R/ec) = 4.51 \times 10^{12} \; A^{-1}.\right]$

2.2.1 Amplitude profiles

(The term "profile" is used for brevity, and should not be confused with the projected density as seen by a wire scanner or an IBS).

One obtains

$$\frac{dN}{dx} = \frac{dN}{dt} \frac{1}{dx/dt}$$

by eliminating t

$$\left.\begin{array}{l} x(t) = y_0 - y(t) \\[2mm] \dfrac{dN}{dt}(t) = -\dfrac{C_1}{\beta} \dfrac{dI}{dt}(t) \end{array}\right\} \quad \frac{dN(x)}{dt} = n_t(x)$$

$$\frac{dN(x)}{dx} = n(x) = \frac{n_t(x)}{dx/dt} = -\frac{n_t(x)}{dy/dt} = \frac{C_1}{\beta} \frac{dI(t)/dt}{dy(t)/dt} \; ;$$

$dy(t)/dt$ is obtained by numerical differentiation from $y(t)$; y_0 is the bump amplitude belonging to the reconstructed beam centre.

The practical computation of $-dI/dt$ makes use of four calibration factors for the electronics involved (see subsection 5.4): Beam transformer, ADC, level adaptor, analog differentiator, multiplexer.

Apart from the physical amplitude profile, in some cases a normalized amplitude profile is of interest: in order to study beam blow-up phenomena on a rising machine cycle, a series of profiles (with incrementing measurement time) in the variable $x_N = (\beta\gamma/\beta_1\gamma_1)^{\frac{1}{2}}x$, $(\beta_1\gamma_1)$ referring to the first profile's beam momentum, is better suited: all profiles should coincide if there is no blow-up.

The actual processing software caters for both kinds of amplitude profile, depending on the timing base chosen: physical amplitudes for the D-train (a 10 kHz clock) and normalized amplitudes for the B-train (bending field in gauss).

Figure 5 shows an example of the use of normalized amplitude profiles, taken from Ref. 12.

2.2.2 Emittance profiles

Sometimes profiles in physical ($\epsilon = x^2/\beta_{CS}$) or normalized ($\in = \epsilon\beta\gamma$) emittance are preferable. They are easily obtained from the amplitude profile $n(x)$

$$n_\epsilon(\epsilon) = n(x)\frac{dx}{d\epsilon} = n(x)\frac{\beta_{CS}}{2x} \; ,$$

and

$$n_\in(\in) = n_\epsilon(\epsilon)/(\beta\gamma) \; .$$

Both displays are provided by the software package.

For operation purposes a "hybrid" display is available: $n(x)$ with an abscissa in physical emittance, i.e. $n[x(\epsilon)] = \tilde{n}(\epsilon)$. Of course $\int \tilde{n}(\epsilon) \, d\epsilon$ is not correctly normalized:

$$\int \tilde{n}(\varepsilon) \, d\varepsilon = \frac{2N}{\beta_{CS}} \langle x \rangle \neq N \, ,$$

but the display is sensitive to variations of the large amplitude tail of the amplitude profile.

2.3 Computation of the bump amplitude

The determination of the computed bump amplitude, one of the three basic Beamscope signals, splits into a linear or lattice part, where the amplitude is calculated from the deflection angles, and a basically non-linear part, namely the calculation of the deflecting angles from shunt voltages. Both steps are straightforward.

The amplitude of the closed-orbit perturbation due to one dipole is given by[13]

$$y(s) = \frac{\theta}{2 \sin \pi Q} \sqrt{\beta_0 \beta(s)} \, \cos \left(\int_{s_0}^{s} \frac{ds}{\beta(s)} - Q\pi \right) \quad \text{for } s_0 \leq s < s_0 + 2\pi R \, ,$$

where β_0 is the β function at dipole position and θ is the deflection angle.

In order to create a local closed-orbit bump, three dipoles are needed, whose deflections have to obey the conditions (see Fig. 6 for nomenclature)

$$r = \frac{\theta_c}{\theta_u} = -\left(\frac{\beta_u}{\beta_c}\right)^{\frac{1}{2}} \frac{\sin(\psi_d - \psi_u)}{\sin(\psi_d - \psi_c)} \, , \quad t = \frac{\theta_d}{\theta_u} = \left(\frac{\beta_u}{\beta_d}\right)^{\frac{1}{2}} \frac{\sin(\psi_c - \psi_u)}{\sin(\psi_d - \psi_c)} \, .$$

The indices u, c, d denote upstream, centre, and downstream dipole location, respectively. If (as was done in the PSB) one places the dipoles on equivalent positions in standard lattice cells, the constraints become simply

$$r = \frac{\theta_c}{\theta_u} = -2 \cos \mu_1 \left(= -2 \cos \frac{\pi Q}{8} \text{ for the PSB} \right) \, ,$$

$$\frac{\theta_d}{\theta_u} = 1$$

where μ_1 is the betatron phase advance per standard machine period: $\mu_1 = 2\pi Q/16$ for the PSB.

The expression for the bump amplitude of three correctly excited dipoles assumes a simple form:

$$y(r) = \theta_u \sqrt{\beta_u \beta(s)} \begin{cases} \sin \Phi & 0 \leq \Phi \leq \mu_1 \\ \sin(2\mu_1 - \Phi) & \mu_1 \leq \Phi \leq 2\mu_1 \\ 0 & \text{otherwise} \end{cases}$$

$$\Phi = \psi - \psi_u = \int_{s_0}^{s} \frac{ds}{\beta} \, .$$

The ideal constraints being only approximately met, the computed bump amplitude has to be summed over the three individual amplitudes (for $\mu_1 = Q\pi/8$):

$$y = y_u + y_c + y_d$$

$$y_u = \theta_u y_1 \cos (\Phi - Q\pi)$$

$$y_c = \theta_c y_1 \cos \left(\Phi + \frac{7Q\pi}{8}\right) \qquad y_1 = \frac{(\beta_{aperture}\beta_{dipole})^{\frac{1}{2}}}{2 \sin Q\pi}$$

$$y_d = \theta_d y_1 \cos \left(\Phi + \frac{3Q\pi}{4}\right)$$

Lattice functions β and Φ are computed by interpolation between stored values for round Q-values, which in turn were computed off-line by a program derived from Saviolakis' computer feasibility studies[7]. Hence the validity of the approximation is limited to working points Q_H, Q_V not too far from the standard quadrant $4 \leq Q_H < 4.5$, $5 \leq Q_V \leq 5.5$.

An improved version now being implemented computes the lattice functions by the matrix method [based on BOOM[14], the PSB specific lattice program].

It remains to calculate the deflection angle θ from the current acquired via the shunt voltage. Since[13]

$$\theta = \frac{\int B \, d\ell}{3.1297 \, \beta\gamma} \, ,$$

we need to know the magnetization curve of the dipoles. Since the 24 individual dipoles (3 stacks) are not fully identical and there is an influence of the position within the stack due to the support, they had all to be measured in the lab, but in their real position within the spare triplet of the PSB, to correctly include fringe-field effects on the integral $\int B \, d\ell$. This quantity was measured[8] for each dipole in pulsed mode for 12 different currents from 0 through 110 A, the limit of the power supply. For processing purposes the curves $\int B \, d\ell$ versus I are approximated by a fourth-order polynomial whose coefficients were found with a least-squares fit (program LSQFIT from the CERN Computer Centre Program Library). The error of the approximation is in general less than 5×10^{-3} (the measurement itself suffers from at least 3×10^{-3} possible error). All the 120 coefficients are stored in the computer software.

The integrated field computed this way is the one without vacuum chamber; it has to be corrected for the distortion due to eddy currents in the metallic pipe. For slow variation of the field B and a circular vacuum chamber, the corrections can be found analytically[15]

$$B_{eddy} = -\dot{B} \, T_{eddy},$$

$$T_{eddy} = \frac{\mu_0 Rd}{2\rho} \left[1 + \frac{1}{3}\left(\frac{R\pi}{2h}\right)^2\right]$$

where R, d, ρ are the radius, wall thickness, and resistivity of vacuum chamber, respectively; 2h is the pole gap width.

With the particular values [there are two types of vacuum chamber[16)]], one obtains (2h = 175 mm):

Dipole location	Diameter (ext.) 2R (mm)	Wall thickness d (mm)	Material	Resistivity ρ ($\Omega \cdot m$)	T_{eddy} (μs)
7L4	140	1.5	Stl.steel AISI 3162 +0.2 N	74×10^{-8}	133.6
8L4 9L4	132	1.5	Inox 304L	70×10^{-8}	128.0

T_{eddy} was measured[8)] to be 120 ± 20 μs for the 132 mm chamber.

The effective field inside the chamber $B_{eff}(t)$ can be written

$$B_{eff}(t) = B(t) - \dot{B}\, T_{eddy} \cong B(t - T_{eddy}) \; ,$$

and it is the last form that is used to compute the effective $\int B \, d\ell$: the whole computed bump is numerically shifted backwards in time by T_{eddy}.

3. INTRINSIC RESOLUTION LIMITS

3.1 Influence of scraping speed

Measurements of transverse beam dimensions by scraping off the circulating beam suffer from intrinsic resolution limits related to the speed of the intercepting device.

In order to quantify this relation, we study a model where a target intercepts a beam in a waist, advancing with constant speed d/T_{rev} towards the beam centre.

A quick glance at Fig. 7 already shows that the interception of all particles having betatron amplitudes y between r and r+dr requires a certain number of revolutions, and that this number depends on the fractional part of the Q_y value: for the (rather special) value q = ⅓, already the fourth cut overlaps the first one and this overlapping goes on for all subsequent cuts. Obviously the whole circumference is scraped off, after n_{max} turns, when $2\phi_{n_{max}} = 2\pi/3$ and $\cos \phi_{n_{max}} = $ = ½ = 1 - ($n_{max}d/r$), $n_{max}d = x_{max} = r/2$.

The case for particles sitting exactly on this fractional q value (corresponding to a third-order stopband) is the most unfavourable one that may occur. In practice it is always masked by the unavoidable Q-spread.

The influence of the resonances is clearly visible on Fig. 8, where x_{max}/r versus q is depicted for several scraping speeds d/r. The "base line" of this diagram, i.e. the off-resonance resolution, is given by

$$\frac{x_{max}}{r} = \frac{1}{2}\left(\frac{3\pi d}{r}\right)^{2/3} \;,$$

which is valid for distances from the resonance M/N:

$$\left|Q - \frac{M}{N}\right| > \left(\frac{3\pi d}{r}\right)^{1/3}/(\pi N) \;.$$

A handy table of this formula was given in Ref. 1.

Results of analytic calculation and computer simulation of the resolution function and its dependence upon the vicinity of a resonance are given in the Appendix. The resolution function itself (see Appendix for definitions) is shown on Figs. 9 and 10.

3.2 Influence of momentum spread

The dispersion of the orbital momentum of the circulating protons, in the PS Booster of the order of $\pm 3\%_0$(trapping) $- \pm 1.5\%_0$(transfer), influences the Beamscope measurement in two ways:

i) It introduces a spread in bump amplitudes of the order of magnitude given above, simply via the magnetic rapidity. This causes a loss of resolution of comparable order, which can certainly be neglected with respect to the effect of the scraping speed and with other error sources (see Section 4).

ii) Radial beam dimensions are the sum of both betatron and momentum amplitudes (in the PSB the momentum compaction function is a smooth function around a mean value of 1.4 m that never vanishes). On the other hand, it is common practice in the PS complex to quote the over-all beam dimensions or emittances, as they are measured straight with targets without any attempt to disentangle the components. The latter is possible in principle with a series of measurements combining targets and Beamscope, say, as described in Ref. 3. In general, however, the total dimension is more useful anyway, since it is related to both the space-charge detuning and the acceptance of a machine.

All measurements and comparisons with targets (see Section 7) were made in this way. This is possible because the horizontal beta function and the momentum dispersion are about proportional to each other in a standard lattice, and therefore the amplitude ratio of the two components is nearly constant throughout the machine period.

A comment is to be made on the validity of the tangent fit described in subsection 2.1.1. If the distributions of momentum and of betatron amplitudes are

independent (a reasonable, but not experimentally proven assumption), one can write for the total amplitude x,

$$x = a + p$$

where

a is the betatron amplitude

$$p = x_p \, (\Delta p/p_0).$$

Suppose a linear betatron amplitude distribution (= const. phase-space density, as assumed in the vicinity of the origin) $f(a) = Ca$, and a finite momentum distribution $g(p)$ with $\int_{-P}^{P} g(p) \, dp = 1$, the distribution of the total amplitude $h(x)$ is given by

$$h(x) = \int_{Max(-P,x-a_{max})}^{Min(P,a_{max})} dp \; g(p)C(x - p) \; .$$

Then $h(x) = Cx$, if a) $x < a_{max}-P$ and $P < a_{max}$; b) $g(p)$ is an even function.

Condition (a) means that for a successful fitting of a tangent to the raw profile's slope, the slope should show a linear course around the fitting point. This condition met, the target should intersect the abscissa right at zero betatron amplitude, if (b) the momentum distribution is symmetric, which is obviously the case for a bunched beam.

Radial measurements of coasting beams with asymmetric momentum distribution result in two different amplitude profiles depending on the polarity of the bump, thus indicating that the interpretation is no longer meaningful. Nevertheless, since the situation at the targets is the same, comparisons with targets still make sense.

3.3 Resolution limits due to finite bandwidth of the signal-processing chain

Disregarding for the discussion the other resolution limits, the beam-derived signals of an ideally hollow beam (represented in normalized phase space by an infinitely thin ring) would be a (downwards) step function for the beam current and a Dirac δ-function-type signal for its derivative. Processing these signals without distortion would require infinite bandwidth. The bandwidth limitation of the real electronics in turn can be expressed as a loss in resolution of the (otherwise ideal) measuring system. In order to quantify the finite resolution, we assume that the limiting element is the beam transformer and that it rolls off with 6 dB/octave (one pole). This corresponds to a transfer function:

$$H(p) = \frac{1/\tau}{p + 1/\tau} \; , \quad p = j\omega \; ,$$

$\tau = 1/2\pi \; f_{3dB}$ being the time constant related to the roll-off frequency f_{3dB}.
Since the δ pulse response in the time domain is given by the inverse Laplace
transform of the transfer function, we obtain

$$h(t) = \mathcal{L}^{-1}\left[H(p)\right] = \frac{1}{\tau} \; e^{-t/\tau} \; .$$

Thus the δ pulse is deformed into a finite-height, exponentially decaying pulse
with time constant τ. The Slow Beam Transformer of the PSB, whose signals are used
for Beamscope measurements, is designed to roll off at 10 kHz, or $\tau = 1.6 \times 10^{-5}$ s =
= 1.6×10^{-2} ms.

To get a spatial measure for the width of the resolution function, we have to
take the quantity $\tau\dot{y}$, with $\dot{y}$ being the scraping speed or speed of the bump ampli-
tude. The latter assumes values between 5 mm/ms (measurements at 800 MeV) and
30 mm/ms (50 MeV), resulting in resolution widths of 0.08-0.4 mm. This is inferior
to the intrinsic resolution limits as given in subsection 3.1 in most cases.

Although it is possible in principle to extend the bandwidth of the system,
attempts to use the "Intermediate Beam Transformer" extending intrinsically to
3 MHz have not given satisfactory results: the markedly increased noise level
demands drastic (digital) filtering during software processing, giving away what
might have been gained at the source.

4. ERROR SOURCES, AS CONCEIVABLE, AND THEIR EFFECT

In this section a number of error sources that are conceivable are checked
against their influence on the accuracy of the measurement. As a general rule,
it has been assumed that individual errors of any kind and in any process should
not exceed 5×10^{-3}.

4.1 Parasitic shaving

The very dangerous effect so termed means that the beam is actually lost on
an obstacle other than the precision collimator made for this purpose. Of course
it is easy to make this collimator so narrow that there is ample margin for all
working points and beam sizes, but the ensuing loss of acceptance would severely
limit machine performance. Since a multitude of parameters intervenes (beam
dimensions, working point, closed-orbit amplitude, ratio of dipole strength), the
trade-off is rather delicate and not straightforwardly found. Any error committed
becomes fatal in the sense that there may be no way to detect it, since the mea-
surement works apparently normally and just the results are wrong.

The feasibility of some possible dipole configuration has been studied by
Krempl in an unpublished work. It has been verified for the dipole positions
chosen in straight sections 7L4, 8L4, 9L4, in an extensive computer study by
Saviolakis[7], covering all working regions that could be envisaged and including the

closed orbit as measured at that time. For the aperture, located in the flange
between pick-up 8RU and quadrupole 8QDU, 70×80 mm^2, or 265×100 (π mm•mrad)^2
in acceptance terms, was considered to be a good compromise, leaving a safety
margin of 4-5 mm in the (critical) vertical plane with respect to the nearest
obstacles (the scrapers in bending magnets 8RB1 and 8RB2). However, by the end
of 1979, it became evident that this aperture is now a limit to a further increase
of intensity, and a modification of the present configuration is to be considered
in the near future.

4.2 Uncertainty in Q values

It has been found experimentally that using the *measured* Q values in the
computation of bump amplitude gives the best fitting emittance measurements. This
corresponds to what one expects, since in both the Q and the Beamscope measurement
the trajectory is deformed and the coherent Laslett Q shift should determine the
effective Q's. However, the Q measurement is suffering from some jitter, and
averaging should be employed to obtain precise Q values. This may take longer
than the actual Beamscope measurement and is thus normally omitted for convenience.
In practice one works with reference data stored on a disk, which correspond
roughly to the intensity of the chosen type of beam. We want to estimate to which
order of magnitude this uncertainty (or any other error) in Q values is tolerable.
From subsection 2.3 we recall the expression for the (ideal) bump amplitude

$$y_{ap} = \theta_u \sqrt{\beta_d \beta_{ap}} \, \sin \Phi$$

differentiating with respect to Q, we obtain

$$\frac{\partial y}{y \partial Q} = \frac{1}{2} \frac{\beta'_{ap}}{\beta_{ap}} + \frac{\beta'_u}{\beta_d} + \Phi' \, ctg \, \Phi \, ,$$

where the prime denotes $\partial/\partial Q$.

Inserting figures for the present working region, $Q_{H,V} = (4.25, 5.35)$, we
obtain

$$\frac{1}{y_H} \frac{\partial y_H}{\partial Q_H} = -0.11 \quad , \quad \frac{1}{y_H} \frac{\partial y_H}{\partial Q_V} = -0.128 \, ,$$

$$\frac{1}{y_V} \frac{\partial y_V}{\partial Q_H} = 0.075 \quad , \quad \frac{1}{y_V} \frac{\partial y_V}{\partial Q_V} = -0.005 \, .$$

Thus typically the quantity $(1/y) \, (dy/dQ) \simeq 0.1$. To respect the chosen limit of
5×10^{-3} for individual errors, an error in the Q determination of $\delta Q \simeq 0.05$ ap-
pears tolerable. This applies to the single-pulsing method (see subsection 2.1.1).
The double-pulsing method (subsection 2.1.2) is more sensitive when the beam

dimension is small with respect to the bump amplitude, so that at ejection energy or for pencil beams a $\delta Q \simeq 0.01$ should be respected. On the other hand, for large beams, as typical for injection measurements, the accuracy of the Q values is not critical at all.

4.3 Magnet inhomogeneity

Since the dipole stacks used by Beamscope to create the closed-orbit bumps are taken from the dipoles originally built and installed for the correction of closed-orbit errors, there was some concern about the quality of their field, in particular for the large off-axis positions reached by the beam during a measurement. For this reason, when the $\int B\, d\ell$ curves were measured, the field quality over their aperture was checked too[8]. Fortunately it turned out that the dipoles do better than expected and the field errors do not exceed 5×10^{-3} and are below that in most cases. So they are not further discussed here, and for more details Ref. 8 should be consulted.

4.4 Finite length of the magnets

In all calculations of bump amplitudes the dipoles are tacitly assumed to be point-like in the azimuth. In order to determine the effect of finite dipole length ℓ, we restrict ourselves to the case of three dipoles in equivalent lattice positions in consecutive machine periods, using the notation and formulae of subsection 2.3. The integration over the distributed deflection $\theta(\sigma)$,

$$y(\sigma) = \theta(\sigma)\sqrt{\beta_\sigma \beta}\, \sin \int_{s_0+\sigma}^{s} \frac{ds}{\beta} \, ,$$

yields approximately for the bump amplitude

$$y = \int_{-\ell/2}^{\ell/2} y(\sigma)\, d\sigma \simeq \sqrt{\beta_0 \beta}\, \sin \Phi \int_{-\ell/2}^{\ell/2} d\sigma\, \theta(\sigma)\left\{1 + \left(\frac{\beta_0'}{2\beta_0} - \text{ctg}\, \Phi\right)\sigma \right.$$

$$\left. - \frac{1 + \beta_0'\, \text{ctg}\, \Phi}{2\beta_0^2}\, \sigma^2 \right\} \, .$$

The term proportional to σ vanishes for even $\theta(\sigma)$, and we obtain

$$y = y_0 \left[1 - \frac{1 + \beta_0'\, \text{ctg}\, \Phi}{2\beta_0^2}\, \langle \sigma^2 \rangle \right] \, ,$$

where $y_0 = \theta\sqrt{\beta_0\beta}\, \sin \Phi$ is the ideal amplitude for point-like dipoles and $\langle \sigma^2 \rangle$ denotes the second moment of the magnetic field distribution,

$$\sigma^2 = \frac{1}{(B\rho)} \int_{-\ell/2}^{\ell/2} B(\sigma)\sigma^2 \, d\sigma \ .$$

From measurement of $B(\sigma)$, $\sqrt{\langle\sigma^2\rangle}$ has been evaluated to be 13.5 cm [17]. With this value the correction term in the square bracket becomes

$$2 \quad \times 10^{-5} \qquad \text{(hor.)}$$
$$-1.5 \times 10^{-4} \qquad \text{(vert.)}$$

and is thus completely insignificant.

4.5 <u>Effect of non-linearities (zero-harmonic octupoles)</u>

We consider only the first-order effect of the "dipole" constituted by the one octupole which is situated closely to the maximum of the bump such that the beam passes at a large distance from the chamber axis. All the other effects of second order as Q shift and lattice function distortion are neglected. With the general expression for the octupole field,

$$Bx = \frac{B'''}{6} (3x^2 y - y^3)$$

$$By = \frac{B'''}{6} (x^3 - 3xy^2) \ ,$$

we obtain the deflection due to that octupole

$$\theta_{oct} = -\frac{\int B''' \, d\ell}{6 \times 3.1297\beta\gamma} \, y_{oct}^3 \qquad (x \simeq 0) \ .$$

Expressed by the bump amplitude at the aperture y,

$$y_{oct} = y\left(\frac{\beta_{oct}}{\beta}\right)^{\frac{1}{2}} \frac{\sin \Phi_{oct}}{\sin \Phi}$$

and the relative error in bump amplitude becomes

$$\frac{\Delta y}{y} = \underbrace{\frac{\int B''' \, d\ell}{37.56 \, \beta\gamma}}_{12(B\rho)} \, y^2 \, \frac{\beta_{oct}^2}{\beta} \, \frac{\cos(\Phi - \Phi_{oct} - Q\pi)\sin^3 \Phi_{oct}}{\sin \pi Q \sin^3 \Phi} \ .$$

Since the octupoles are not powered at injection, their effect intervenes mainly at measurements at 800 MeV, when the octupoles are excited to their maximum strength $\int B''' \, d\ell = 80.4$ T/m^2. In this case, one obtains with the PSB parameters on the normal working point:

Plane	Error in bump amplitude	
	Relative (%)	Absolute (mm)
Horizontal	1.4	0.49
Vertical	1.8	0.72

For the time being this error is accepted and no correction is attempted. For comparison measurements with targets, the octupoles are de-energized just prior to the measurement. With the future transverse feedback system there will be no need for them anyway and this error source will disappear.

4.6 Position errors -- errors in lattice functions

Since beam dimensions are derived directly from the computed bump amplitude, it is of some interest to know the sensitivity of the latter to errors in the parameters used. These errors may be classified as follows:

a) "Surveyor's error", i.e. errors in the positioning of dipoles and aperture, or in their assumed positions.

b) Deviation of the real lattice functions from the "ideal" or computed ones. All computations rely on correct idealization of the real magnets and, even if this is well done, real lattice functions in the fringe field zone of a magnet may still deviate from calculations. This is very likely to be the case for the aperture, which is inserted into the vacuum chamber flange of the defocusing quadrupole. In addition to this, the lattice functions may be distorted by errors in the alignment of the focusing elements.

c) "Excitation errors" of the dipoles, which may be due to calibration errors in shunts or electronic processing, or in the underlying measurement of $\int B \, d\ell$ versus dipole current, or due to field inhomogeneity.

The following formula allows one to determine the individual weights of the different types of errors. Instead of the ideal bump amplitude,

$$y(\Phi) = y_0 \sin \Phi$$

where

$$y_0 = \theta \sqrt{\beta \beta^{\text{dipole}}}$$

and

$$\Phi = \int_{s_0}^{s} \frac{ds}{\beta} \, ,$$

one can write for the perturbed bump amplitude:

$$y(\Phi) = y_0 \left[1 + \frac{\Delta y_0}{y_0}\right] \sin(\Phi + \Delta\Phi) \; ,$$

with

$$\frac{\Delta y_0}{y_0} = b + \frac{1}{2}\left[e_u + S_c e_c + S_d e_d + \text{ctg } \pi Q \; \phi_u - C_d \phi_d\right]$$

$$\Delta\Phi = d\Phi + \frac{1}{2}\left[\text{ctg } \Phi \; e_u + C_c e_c + C_d e_d - \phi_u - S_d \phi_d\right] \; .$$

Subscripts u, c, d refer to the upstream, centre, and downstream dipoles.

Constants are given together with their computed values for $Q_{H,V} = (4.2, 5.3)$:

$$S_c = -r \frac{\sin \frac{7}{8} \pi Q}{\sin \pi Q} = (\,0.228, \quad 1.097) \qquad r = -2 \cos \frac{\pi Q}{8}$$

$$S_d = -\frac{\sin \frac{3}{4} \pi Q}{\sin \pi Q} = (\,0.772, \; -0.097)$$

$$C_c = r \frac{\cos \frac{7}{8} \pi Q}{\sin \pi Q} = (\,0.139, \quad 0.506) \qquad \text{ctg } \pi Q = (1.376, \; 0.726)$$

$$\qquad\qquad\qquad\qquad\qquad\qquad\qquad\qquad \text{ctg } \Phi = (0.235, \; -0.464)$$

$$C_d = \frac{\cos \frac{3}{4} \pi Q}{\sin \pi Q} = (-1.516, \; -1.232)$$

(These expressions are valid only for the PSB lattice with a phase advance of $\mu_1 = \pi Q/8$ per machine period.)

The errors b, $\delta\Phi$, $e_{u,c,d}$ can be split as follows:

$$2b = \frac{\delta\beta + \beta'\delta s}{\beta} \qquad \text{error in } \beta \text{ function at the aperture (intrinsic + due to position error } \delta s)$$

$$d\Phi = \delta\Phi + \frac{\delta s}{\beta} \qquad \text{error in phase at the aperture (intrinsic + due to position error } \delta s)$$

$$e_{u,d} = \frac{\delta\theta_{u,d}}{\theta} + \frac{\delta\beta^{\text{dipole}}_{u,d}}{2\beta^{\text{dipole}}} + \frac{\beta'^{\text{dipole}}}{2} \phi_{u,d}$$

$$e_c = \frac{\delta\theta_c}{r\theta} + \frac{\delta\beta^{\text{dipole}}_c}{2\beta^{\text{dipole}}} + \frac{\beta'^{\text{dipole}}}{2} \phi_c \; .$$

$e_{u,c,d}$ are the total errors due to dipoles: $\delta\theta_{u,c,d}$ are the total excitation errors, and the two remaining terms the error in β-function, again the intrinsic one and the one due to the position error: $\phi_{u,c,d} = \delta s_{u,c,d}/\beta^{\text{dipole}}$.

In its general form the formula is rather academic, but the influence of the individual errors can be easily identified.

5. HARDWARE

5.1 Dipoles

As already stated in the Introduction, three stacks of standard PSB ring di-
poles, initially foreseen for closed-orbit correction, have been dedicated for
Beamscope. This was possible after extensive measurements in pulsed mode[8] revealed
a very satisfactory homogeneity of their field across the useful aperture even in
the regime of beginning saturation. The detailed description of these stacks
termed "Type 1" dipoles, each one containing four (double: hor. and vert.) dipoles,
is given in Ref. 9 and in the Technical Specifications (Ref. 18). Originally speci-
fied for d.c. operation at a nominal current of 10 A and maximum ratings of 15 A,
the dipoles are pulsed in operation up to 90 A and have been measured up to 110 A
peak current, with a half-sine pulse of length about 20 ms. The duty cycle is very
low. The minimum repetition interval to be expected is 1.2 s. Their characteristics
are:

$$L_{hor.} = 74.5 \text{ mH} \qquad \int B \, d\ell_{hor.} = 7.3 \times 10^{-3} \text{ T·m}$$

$$L_{vert.} = 66.3 \text{ mH} \qquad \int B \, d\ell_{vert.} = 7.2 \times 10^{-3} \text{ T·m}$$

$$R = 1.12 \, \Omega \qquad \text{for 10 A excitation.}$$

5.2 Power supplies and multiplexer

The three pulsed power supplies are based on thyristor-controlled capacitor
discharge. Derived from power supplies developed for the New Linac, they have been
built at CERN by M. Bourgeois. Matched capacitor banks of 800 μF can be charged up
to 1000 V, allowing for peak currents in the dipoles of $\gtrsim$ 100 A within 10 ms. The
relay-based switchyard connecting the three power supplies to any set of three di-
poles belonging to one ring and one plane is controlled by a NIM module (in the
Main Control Room), which also permits the (manual) control of the amplitude of
the discharge bump. The absolute amplitudes of the upstream and the downstream
dipole are equal and thus controlled in parallel, whereas for the central dipole
the relative amplitude with respect to the outside ones is controlled separately
for each plane, corresponding to the different deflection strengths and ratios
$r = \theta_c/\theta_u$ (see subsection 2.3) required. Besides this, the module allows selection
of ring, plane, and polarity of the bump manually or by remote control via the old
CERN-made STAR transmission system. At present a CAMAC/STAR interface allows con-
trol via the Serial CAMAC of the T-BMC, the temporary beam measurement computer.

A feature of the power supplies is that there is the possibility to dump the
capacitor discharge into a crowbar, whenever an external condition, the so-called
stop-pulse, arrives. This stop-pulse is generated by a comparator module (also
in the Main Control Room), detecting the passage of the beam current through 95%

of its value at the start of the Beamscope measurement. This feature is currently used in the double-pulsing measurement mode (see section 2.1.2) to stop the rising bump once the 95% amplitude has been found and avoid total beam loss.

The switchyard and the controller module was built at CERN by C. Carter and the comparator by L. Magnani. For the transfer of Beamscope to the new control system of the PSB, the controller will have to be rebuilt; the layout of the future "standard interface" is described elsewhere[19]. A note describing the specific interface, and covering also the power supplies, is in preparation[20].

5.3 The aperture

The precision aperture, although a comparatively simple and "invariant" part of the system, nevertheless merits some investigation because of its role as acceptance limitation and loss absorber at lower energies, and its influence on the irradiation of the machine. The details of these considerations exceed the scope of this paper and will be given in a dedicated note[21]. Here just a few criteria for its choice are summarized.

In order to be able to measure beams filling the available acceptance of the machine (this case occurs with a high-intensity beam at injection energy), the Beamscope aperture must be *the* acceptance limitation. This means that all particles lost during capture and acceleration hit this collimator, which determines where they are ultimately lost. To preserve the resolution of the measurement, one is interested in losing the intercepted particles as rapidly as possible, in order not to further reduce the intrinsically limited resolution (see section 3). This excludes the otherwise preferable solution of a diffuser foil with a massive dump suitably downstream. As a compromise, a thickness was chosen such that most of the protons up to 70 MeV are stopped. Beyond that energy, multiple scattering within the collimator causes sufficient emittance increase that the particle is lost within a few turns even at top energy (800 MeV). A thickness of 15 mm of copper does this job, the copper also assuring good thermal conductivity as required to avoid inadmissible temperatures at the intercepting edge of the collimator. Copper is not the best choice for low induced radioactivity; this appears, however, tolerable when easy mechanical exchange is foreseen. Graphite, a barely activated material, would on the other hand require an intolerably high thickness of the collimator: although the edge of the aperture is matched to the slope of the beam envelope, the position and width of the aperture would no longer be precisely definable. The dimensions of the aperture are given in subsection 4.1.

5.4 CAMAC crate and computer configuration

Beamscope and some other measurement systems became feasible once the PSB Beam Measurement Computer (T-BMC, the T standing for "temporary", awaiting something equivalent in the frame of the new control system) and its CAMAC loops came into

operation on the initiative of C. Metzger. The T-BMC configuration having been described elsewhere, we just reproduce its layout in Fig. 11 (taken from Ref. 22). Beamscope requiring the graphics facilities, it can be operated from either one of the Tektronix 4014 terminals in the Main Control Room (MCR) or the Booster Observation Room (BOR).

One CAMAC crate in the BOR houses all the equipment for acquisition of the five raw analog signals (Fig. 2) plus the preset counters. Multiplexing and (exclusively manual) reference setting of the three power supplies is controlled from the MCR by the "Beamscope Controller", a NIM module with manual or remote control via STAR, the old PS data transmission system. The module is now linked to the T-BMC via a CAMAC/STAR interface in crate 60 (Fig. 11).

Figure 12 shows the functional configuration of the CAMAC modules. All five analog signals may vary in amplitude, and level adaptors, being actually home-made programmable amplifiers (gain variation by a factor 10 in four steps) are required to coarsely match the signal level to the input range (0-1 V) of the ADCs. The latter are of the 10-bit sampling type with max 1 MHz sampling frequency and 1 k memory (SA/D 1001 from Standard Engineering Corp.). Another home-made module is the "timing selector", allowing the measurement of a required type of beam in a ppm (pulse-to-pulse modulation) operated PSB; in fact a gate for the measurement trigger controlled by the logical product of all external conditions. The physical layout is depicted in Figs. 12 and 13, taken from Ref. 11.

6. SOFTWARE

6.1 "Philosophy" and organization

Bearing in mind the complexity of PSB operation and the ensuing variety of beam properties, it is perhaps not too surprising that the development of the software package was the most tedious and time-consuming part of the total manpower required.

The PSB consists of a stack of four simultaneously operated accelerators whose intensity is modulated from pulse to pulse (periodically within one "supercycle"). There is only one set of hardware which is multiplexed (except the dipoles, of course) to measure the desired ring and plane. To lock the measurement to a certain type of cycle, the hardware is controlled by "Intensity Program Lines (1 ... 8)", so-called IPLs (in future "USER" lines). This means that "measurement parameters" have to be defined by the user.

Measurement parameters:

Parameter	Range	Description
IPL	1-8, ALL	"Intensity Program": labels a type of machine cycle with characteristic beam properties.
Ring	1-4	
Plane	H, V	
Timing	2 trains (B,D). 4 reset pulses. Pulse No.	Defines the beginning of the measurement by a pulse of one of the trains and the reset pulse of the preset counter.
Q_H, Q_V		Coherent Q values to be found by a Q measurement at the timing defined above.
B (G)	1256-5920	Magnet bending field proportional to beam momentum. Automatically defined by B train; to be entered manually when on flat top (D train).

Once the set of measurement parameters has been defined by the user, another set of parameters has to be found, termed here as "process parameters". These parameters can be compared with the settings of an oscilloscope, such as sensitivity, sweep, and delay, that have to be manipulated in order to get a reasonable trace on the screen, centred on the event one wants to observe. In our case the screen is replaced by the memory of the ADCs, the sweep corresponds to the sampling rate, and the sensitivity may be adapted to the signal by controlling the gain of the level adapters (see subsection 5.4).

Since there are five signals and the settings may vary with ring, plane, polarity of the bump, and, of course, beam type (IPL) and energy, a routine measurement could easily degenerate into an experiment. Fortunately, emittance measurements are systematically done at specific timings and energies, roughly corresponding to injection and ejection, and also the various beam intensities are classified by IPL numbers. The way out of the dilemma is thus given by systematic storage on disk of every process parameter found plus all its subsequent modification, for injection and ejection energy. In fact there are two disk files for these standard measurements plus one more for storage of data relevant for another, experimental, situation.

The main process parameters are:

Process Parameters

Parameter	Multiplicity					Possible No. of values	Remarks
	IPL	Ring	Plane	Polarity	Channels		
Beam transformer	9					3	1) intermediate BT 2) slow BT 3) normalized BT
Level adapter setting	9		2		5	4	4) gains: 1, $\frac{1}{2}$, $\frac{1}{5}$, $\frac{1}{10}$
Acquisition delay	9	4	2	2		any > 0	delay between start of bumper supplies ("FIRE" pulse) and start of digitizing (in μs)
Sampling interval	9		2			any ≥ 1	in μs; total sampling time $\simeq 1000 \times$ sampling int.

On top of these 261 parameters, the measurement parameters -- in particular timing and beam energy -- and more than a hundred "software parameters" are saved on disk. The latter comprise calibration factors, as for ADCs, level adapters, beam transformers, coordinates for graphics displays, scale factors, smoothing parameters, flags for debugging helps, etc. They can be altered on-line by the operator.

This concept has proved to be very useful in operation. It is backed up by a routine AUTOSCOPE that automatically adjusts the process parameters whenever changed beam parameters require their modification.

Other parameters stored in the computer code itself are the coefficients of the power series fits to the magnetization curves of all 24 dipoles involved. The polynomial approximation of the lattice function is now replaced by the exact calculations using the program BOOM[14] recently implemented on the T-BMC.

Use of rather extensive calculations has only become possible since the program package has been split into three real-time (RT) programs: the main RT program BSCOP plus the "conversation" program BSCO1 to define measurement parameters; and now BSCO2, calculating lattice functions with the help of the BOOM Library. The RT programs communicate via reserved areas in resident COMMON. The fact that, unsplit, the code exceeds the virtual address space of the 16-bit system is to be explained by the complexity of the Tetronix PLOT-10 Advanced Graphing System, occupying almost half of this space.

The program package is written in NORD-10 FORTRAN, except the non-specific routines used, as the Serial CAMAC driver, written by W. Remmer in NORD-PL.

6.2 Short description

Here we sketch just the structure, as seen by the user, of the program package. A detailed description of the individual routines is available for the users[23]. The program can be entered from any terminal via the START-APPLICATIONS facility[24]. It automatically responds by presenting the "menu" of all facilities for the "EJECTION" set of parameters (Fig. 14). Here one can distinguish four groups of subprograms:

i) *Operation programs:* They provide a "scan" of the emittances of one or all rings, optionally complemented by the amplitude profiles of the preselected timing stored in the file. Figure 15 shows a typical output for four rings. When run repeatedly, emittance values (last shot and cumulative average) are displayed in refresh mode.

ii) *Programs for machine experiments:* They provide detailed profiles or profile series of various kinds, normalized or not, as indicated in subsection 2.2. Illustrative examples are Fig. 5 and Fig. 16, the latter showing a display option. Program No. 11 engages a conversation to alter measurement parameters.

iii) *Utilities:* Their need has been recognized in the course of the development of the measurement system. There are routines for manual (21,22) or automatic (28) setting of the process parameters, for copying settings from one program line onto another (24) and to swap files (EJECTION, INJECTION or EXPERIMENT) as explained in subsection 6.1. The "Library Program" is one out of several maintenance programs selected at compilation stage, the virtual address space being too restricted to allow for all of them.

iv) *Emittance measurement/target comparison:* Programs performing emittance measurements that can be monitored in all phases, comparing both methods (subsection 2.1) with each other and (optionally) with target measurements. The various errors are computed and displayed. Optionally the data may be written onto disk for subsequent postprocessing, as described in section 7.

If desirable, one can inspect and interactively modify the tangent fit required for single pulse emittance measurement. This can be seen on Fig. 17, showing a display of this program group.

7. COMPARISON MEASUREMENTS: BEAMSCOPE VERSUS TARGETS

7.1 Method of analysis

Glossary

x	true beam radius (95%) at the aperture.
x^t	true beam radius at the target.
$x_{I,II}$	x measured by Beamscope with single- (I) or double-pulse (II) method.

x_T^t measured by targets and subsequently reduced to

x_T (at the position of the aperture) by multiplication with $s = \sqrt{\beta_A^0/\beta_T^0}$.

β_i^0 theoretical (from lattice computation) value of β-function at i.

a   half aperture.

$y_{1,2}$ true bump amplitudes.

$y_{1,2}^0$ computed bump amplitudes.   } for the two polarities 1,2.

$y_{a_{1,2}}$ bump amplitudes for zero beam radius (reconstructed)

$$\alpha = \frac{\delta\beta_A}{2\beta_A^0} , \quad \delta = \frac{\delta\beta_D}{2\beta_D^0} \text{ (mean over the three dipoles), } \quad \tau = \frac{\delta\beta_T}{2\beta_T^0} ,$$

relative errors in the β-functions at aperture, dipoles, and target with respect to the *computed* β-values β_i^0.

ε relative error in $\int B \, d\ell$ measurement and in calibration of electronics, with respect to computed bump amplitude.

t^t offset type error in target measurement, t reduced to aperture.

o   error (absolute) in c.o. reconstruction.

In the following calculations, only first orders in errors are kept; higher-order terms in errors are systematically discarded.

Note that the errors used here are defined in an opposite way to the usual one: they are defined as the differences of the real values from the computed ones.

We express the measured quantities by the true ones:

Target

$$x_T^t = x^t + t^t$$

$$x^t = \sqrt{\beta_T/\beta_A} \ x = \sqrt{\beta_T^0/\beta_A^0} \ (1+\tau-\alpha) \ x$$

$$x_T = x_T^t \ s \quad , \quad t = t^t s$$

$$x_T = x(1+\tau-\alpha) + t$$

Single-pulse measurement

$$x_{Ii} = y_{a_i}^0 - y_i^0$$

$$x = y_{a_i} - y_i$$

$$y_i = y_i^0 \, (1+\alpha+\delta+\epsilon)$$

$$x_I = \frac{x}{1 + \alpha + \delta + \epsilon} + o \simeq x(1-\alpha-\delta-\epsilon) + o$$

Double-pulse measurement

$$2x_{II} = 2a - (y_1^0 + y_2^0)$$

$$2x = 2a - (y_1 + y_2) = 2a - (y_1^0 + y_2^0)(1+\alpha+\delta+\epsilon)$$

$$x_{II} \cong x(1-\alpha-\delta-\epsilon) + a(\alpha+\delta+\epsilon)$$

From these expressions one derives the quantities

Absolute errors

$$x_I - x_T = o - t - (\delta+\tau+\epsilon)x$$

$$x_{II} - x_T = -t + (\alpha+\delta+\epsilon)a - (\delta+\tau+\epsilon)x$$

$$x_{II} - x_I = -o + (\alpha+\delta+\epsilon)a$$

To first order, one can replace x on the r.h.s. by x_I or x_{II}.

Relative errors

Again to first order, the relative errors are found straightforwardly:

$$\frac{x_I - x_T}{x_I} = -(\delta+\tau+\epsilon) + \frac{o-t}{x_I}$$

$$\frac{x_{II} - x_T}{x_{II}} = -(\delta+\tau+\epsilon) + \frac{o - t + (\alpha+\delta+\epsilon)a}{x_I} \, .$$

The relative error of the corresponding emittances is just twice the r.h.s. The absolute errors of measurements of beams with various dimensions should fall on a straight line in a plot of these errors as a function of x, whose intersection with the y-axis represents the target error (assumed to be of offset type) and the slope yields $\delta + \tau + \epsilon$; $(\alpha+\delta+\tau)a$ is the distance between x_I and x_{II}.

Essentially the same information can be obtained from a plot of relative emittance errors versus 1/x (Fig. 18). Here the straight lines fitting the single- and double-pulse errors should intersect on the y-axis at $-2(\delta+\tau+\epsilon)$. This gives an additional constraint and thus facilitates the fitting. The slope of the single pulse (I) straight line equals -2t, whereas the angle between the two straights is given by $2(\alpha+\delta+\epsilon)a$. Whenever $\alpha + \delta + \epsilon \neq o$ the two measurements I, II differ. In fact, $\alpha + \delta + \epsilon$ is the relative error of the computed bump amplitude. It can even be determined without any target measurement by comparing the "reconstructed"

aperture value with the physical one. The former is obtained by adding the bump
amplitudes for zero beam radius $y^0_{a_1} + y^0_{a_2}$ for the two polarities (assuming o = 0):

$$y^0_{a_1} + y^0_{a_2} = (y_{a_1} + y_{a_2})/(1+\alpha+\delta+\varepsilon) = \frac{2a}{1 + \alpha + \delta + \varepsilon} .$$

In order to compensate for the unavoidable (systematic) errors $\alpha + \delta + \varepsilon$, one can
numerically adjust the calibration such that $y^0_{a_1} + y^0_{a_2} = 2a$, i.e. multiply the
computed bump amplitudes by the factor $1 + \alpha + \delta + \varepsilon$ found from aperture reconstruc-
tion. After this correction $\alpha + \delta + \varepsilon' = 0$, and the results of both measurements
should agree by virtue of

$$x_{II} - x_I = (\alpha+\delta+\varepsilon')a$$

and the data points of both relative errors should fall on one single straight
line. This new straight line is parallel to the uncorrected line I (slope o-t)
but displaced by $\varepsilon' = -(\alpha+\delta)$. Its intersection with the y-axis gives

$$-[\delta + \tau - (\alpha+\delta)] = \alpha - \tau .$$

Systematic measurements thus allow one to determine relative errors of β functions:

$$\alpha - \tau , \alpha + \delta$$

and systematic target errors $t^t = t\sqrt{\beta^0_T/\beta^0_A}$ where we neglected ε and o.

7.2 Experimental results

The analysis exposed in the preceding paragraph will here be demonstrated on
a series of measurements in Ring 3. Horizontal and vertical target measurements
were performed on the 800 MeV flat top, after the synchronization (of the RFs of
the four rings) is finished. Four different test beams per plane, with dimensions
varying as widely as possible, were shaped by the "shavers" (pulsed dipoles for
controlled emittance and intensity reduction, driving the beam into the Beamscope
aperture restriction).

The principal difficulty of these target measurements consists in the inter-
pretation of the loss pattern provoked by the interception. As Figs. 1 demonstrate
there is not a well-defined loss that can easily be tuned to 5% by adjusting the
target position. In fact at least two, sometimes more, loss phases can be distin-
guished. From target monitoring signals (see Fig. 22) one can infer that the
first loss, occurring 35 ms after the target trigger, corresponds to the plunging
of the target arms through the beam. Subsequent losses are probably due to
residual vibrations of the arms, theoretically at rest in fully plunged positions.
In addition, one cannot completely exclude a reaction of the beam (e.g. via the
Beam Control System) to the loss.

Finally, it is not obvious which loss can be related to the calibration of the targets, which was done by interception of a pencil laser beam on the bench.

To deal with all these unknowns, Beamscope measurements have been compared with two different interpretations of target results; consequently there are two sets of measured points in the scatter plots of Figs. 20, taking either the first loss or the second loss for the correct one.

Discussion of results

Figures 20a(b) show the error in the reconstructed horizontal (vertical) aperture for the uncompensated and the compensated data. As explained in subsection 7.1, compensation means that a calibration error ε' has been deliberately introduced so as to make the aperture reconstruction correct. These diagrams allow one to read immediately the compensations ε':

$$\varepsilon'_{hor.} = 2.5\% , \quad \varepsilon'_{vert.} = 1.1\% .$$

Figures 20b,c show the relative emittance error versus 1/beam radius obtained by single- (I) and double-pulse (II) methods for first and second target loss, respectively. (To first order, the relative emittance error is just twice the relative amplitude error used in the analysis.)

Straight lines fitted through the corresponding clusters of points must intersect on the vertical axis (this means that all target measurement errors vanish when related to a beam of infinite radius).

Figures 20e,f display the same data after application of the compensation as found from Figs. 20a,b. The two straight lines I and II have now collapsed into a single one: single- and double-pulse data now virtually coincide.

Following subsection 7.1 and Fig. 18, we obtain (ε and o neglected, which is a reasonable assumption)

Ring 3	Horizontal	Vertical
$2(\alpha+\delta)$	2.5%	1.1%
$2(\alpha-\tau)$	$-$ 9%	21%
t^t (1st loss)	0.11 mm	0.36 mm
t^t (2nd loss)	0.46 mm	0.94 mm

These results reveal reasonable and, for the horizontal target, even small systematic target (offset-type) errors, when the first loss is taken to be the representative one. But the measurement also suggests substantial errors $\alpha - \tau$ in the conversion factor $\sqrt{\beta^0_A/\beta^0_T}$, probably due to deviations of the true lattice functions from the computed ones.

This leads to the paradoxical effect that for large beams the second-loss interpretation of target measurements gives better agreement with Beamscope. With perfect targets, relative differences between Beamscope and target emittances will be just $2(\alpha-\tau)$ and thus of the order of -9 or 21%, respectively. Since there is no simple means of measuring β-functions and phases in the PSB, it is not possible to tell which kind of measurement is the better.

What is done in practice is just to adjust the compensation of ϵ' such as to make the aperture reconstruction correct to ensure identical results for single- and double-pulse measurements and quote the results found as "Beamscope emittances". As explained, they may differ from "target emittances" owing to the effect of lattice function errors and to the ambiguity in the interpretation of target-induced loss.

8. EXAMPLES OF APPLICATIONS

8.1 Standard applications

The standard application is the operational measurement of transverse beam emittances, complemented by a display of betatron amplitude distributions, as already given in Fig. 15. The latter is important particularly for measurements at injection, where the amplitude distribution affects the achievable performance of the machine.

Detailed amplitude profiles or series of profiles, being available with different display options (Figs. 5 and 15), are useful for the identification and compensation of stopbands. Also the filling of the apertures during the injection process can be monitored and improved "on-line".

8.2 Measurement of two-dimensional amplitude (emittance) distributions

Knowledge of the two-dimensional amplitude distribution $n(a_x, a_z)$ right after injection resp. trapping is of particular interest for a space-charge limited machine such as the PSB: shaping this distribution by various techniques was a major contribution to the rise in machine performance in the last years[25]. Some of the achievements empirically found could be explained from the two-dimensional amplitude distributions measured.

The principle of the method is straightforward: one has a target progressively plunging in one plane while taking a series of Beamscope profiles in the other. In the computer, the differences between the successive profiles are evaluated to produce a matrix of $N \times N$ cells in a_x, a_z space (N being the number of profiles belonging to different target interceptions covering the range of vanishing to maximum amplitudes). The number of protons in each cell is computed and given. Of course this method critically depends on pulse-to-pulse stability of the beam.

The projections $n(a_{x,z}) = \int n(a_x, a_z)\, da_{z,x}$ of the matrix on the x, z axis give histograms of N bins which should coincide with Beamscope amplitude profiles in the x, z plane, respectively. This is illustrated in Fig. 21. A further check of the validity of the measurement technique consists in having the target of the same plane plunging as the Beamscope profile is taken: in this case only the main diagonal of the matrix should be filled. In principle, it should not matter which plane is used by the target and which one for Beamscope. In practice, however, and in particular early in the machine cycle, significantly different results were obtained for the two combinations. In addition, matrix projections agreed better with the Beamscope profile in the vertical plane. The explanation of the discrepancy suggests the presence of coupling between the two transverse planes: for difference resonances, $mE_x + nE_z$ are constants of the motion (E_x and E_z are emittance variables, m and n are integers). It is easily seen that such a beating distorts the measured two-dimensional distribution in the sense that each particle is intercepted at its maximum beating amplitude in the plane of the (comparatively slowly plunging) target. Moreover, for n > m, the beating has less effect on the result obtained with vertical target and horizontal Beamscope measurement than on the other combination, and vice versa.

Nevertheless, fairly consistent measurements were performed with high-intensity beams. From the matrices obtained, one can complete (off-line) the maximum Laslett space-charge detuning. The results obtained with different types of beams confirm that the PSB intensity is always limited by its peak incoherent Laslett Q-shift[25]. At present, the target has to be controlled manually. This is not a decisive drawback since the duration of a measurement is still negligible compared to the preparations and checking procedures (note, as an example, that finding the target position corresponding to the centre of the beam is a tedious exercise).

8.3 Investigations on target functioning

Profile series taken during the target plunging and/or interception phase allow one to gain some insight into the behaviour of the individual targets. The target, a pair of long-armed forks where the distance between the arms can be set individually, swings laterally into the beam, is supposed to stay quietly in intercepting position, and swings out afterwards, according to the velocity program indicated in Fig. 22. Figure 23 depicts a case where the target, after the phase of plunging into the beam ($\sim$ 2 ms), still undergoes slow motion towards the beam centre, as can be seen from the profiles as well as from the beam transformer signal: the latter shows two phases of rapid and slow loss. Obviously the position of the target is not well defined owing to its unprogrammed vibrational motion during the interception phase. Note the finite slope of the intercepted beam edge: it corresponds to the intrinsic resolution limits of Beamscope as described in Section 3. Also remarkable is the pulse-to-pulse stability of the PSB beam at ejection.

8.4 <u>Determination of closed-orbit amplitude</u>
<u>at the Beamscope aperture</u>

As explained in subsection 2.1.1, the single-pulse method yields as a by-product the amplitude x_{co} of the closed orbit. Performing a complete measurement [for example, using the program "Emittance measurement/target comparison (33)"] of the menu (see subsection 6.2 and Fig. 14), this quantity is printed out. It is of some importance because the Beamscope precision collimator constitutes at the same time *the* acceptance limit of the PSB; a non-negligible closed-orbit amplitude at this azimuth automatically reduces the maximum achievable performance (see Ref. 25). Since there is no pick-up right at the collimator, any correction of the closed orbit at this point can only be monitored by Beamscope.

9. <u>POSSIBLE IMPROVEMENTS, RELATED CONSTRUCTIONS, OUTLOOK</u>

9.1 <u>Possible improvements of the existing system</u>

Apart from the continuous small improvements to the hardware and software, a few more substantial modifications seem desirable:

a) computer control of the references of the power supplies (at present set manually);

b) automated Q-measurement prior to a Beamscope measurement [at present being typed in: not too much bother, since the working point hardly changes, and the specific values are stored on the disk files (see Section 6)].

c) speeding up execution by introduction of local (in the CAMAC crate) LSI processors, thus reducing the data load on the CAMAC dataway.

Improvements (a) and (b) are foreseen, at least in principle, for the Beamscope version converted to the new control system; (c) may become unavoidable if the FEC of the PSB in the new control system is too heavily loaded.

9.2 <u>Related constructions</u>

As far as I know, the only existing device comparable to Beamscope is the "Fast Rotary Scraper" of the 12 GeV KEK Proton Synchrotron[26]. A finger on a rotating arm is moved into the beam by means of a stepping motor. Ensuing beam loss is recorded by a beam current transformer, the finger position by means of a precise linear potentiometer.

Mechanical interception of the beam looks *a priori* more attractive than driving the beam into a fixed collimator. In fact, this approach was already envisaged when the implementation of Beamscope began. The idea was rejected, however, mainly because the PSB is actually four machines, and multiplexing three fairly simple power supplies between the already existing dipole stacks was obviously cheaper. In the common case of a single-ring machine, the mechanical approach appears more

advantageous. It eliminates, in any case, a lot of error sources as well as acquisition and computing effort for the calculation of the bump amplitude of our "electromagnetic" approach.

Interception of the beam with a carbon fibre[27] or thin wire[28], although mechanically comparable with the KEK device, essentially differs from Beamscope in yielding the projected density instead of the amplitude distribution. This drawback is counterbalanced by the negligible beam loss caused by this type of monitor.

9.3 Outlook

The mechanical resemblance between carbon-fibre monitors and mechanical "Beamscope" realizations suggests unification or multiple use of the driving mechanism for both devices. But it is only consequent to go one step further: in today's fully computer-controlled accelerators, the classical concept of a measurement target with expensive precision drive is hardly justified -- even more so as the precision of these drives together with that of the position transducer (e.g. a linear potentiometer) was not always as high as one might believe. The more promising approach for new developments appears to be a cheap, smooth, but not precise driving mechanism complemented by an optical position sensor, which acquires the actual instantaneous position of the target. The position can then be sampled at will and this information used for a servo-loop controlling the drive. In this way any desirable motion (at rest at a given position, fast or slow interception) can be realized. Such a device, which I would call a "General Target System", could perform common target measurements, fast Beamscope emittance measurements and amplitude profiles, and/or, when equipped with a carbon fibre, low-loss density-profile measurements too.

A schematic and oversimplified sketch of such a General Target is given in Fig. 22. The rectilinearly moving system shown for clarity may well be inferior to a rotatory one, requiring less bellows contraction. Here an electromagnetic (linear) motor or a pneumatic (no e.m. fields perturbing the beam) drive is controlled by a microprocessor or hard-wired logic. Position is acquired by optical or fibre-optical reading of binary coded length marks, directly applied on the main rod. The structure has to be sufficiently rigid that vibration amplitudes stay below the required resolution. The carbon-fibre detector can intercept the beam when the main rod is turned around. But even if this complication is to be avoided, obviously the same system is suitable for both the carbon-fibre detector and the General Target System. It is very likely that the cost of such a multiple-application device is substantially less than the sum of costs of separate devices.

Acknowledgements

REFERENCES

1) H. Schönauer, Beamscope -- A novel device for measuring emittances and beta-tron amplitude distributions, CERN/PS/BR 79-8 (1979) and IEEE Trans. Nucl. Sci. NS-26, 3294 (1979).

2) P.W. Krempl, The Abel-type integral transform with the kernel $(t^2-x^2)^{-\frac{1}{2}}$ and its application to density distribution of particle beams, CERN MPS/Int.BR/74-1 (1974).

3) J.M. Peterson and J.B. Rechen, A method of analysing the momentum and beta-tron amplitude distributions in a circulating beam, IEEE Trans. Nucl. Sci. NS-20, 790 (1973).

4) P.W. Krempl, PSB Machine Experiment News Nos. 88, 107/114, 126B (1975), and private communication.

5) H. Schönauer, PSB Machine Experiment News, 7.4.77; Comptes Rendus du Comité d'Instrumentation No. 8, 29.4.77.

6) H. Schönauer, PSB Machine Experiment News 27.4.77.

7) A. Saviolakis, Numerical investigation of the feasibility of Beamscope mea-surements without parasitic shaving in the PSB, CERN/PS/BR 77-35 (1977).

8) A. Arn, M. Battiaz and C. Schnell, PSB dipoles, CERN SI/note MAE/72-3 (1972).

9) M. Chanel and G. Suberlucq, Mesures magnétiques de dipôles d'anneau Booster Type 1 en régime pulsé, CERN/PS/BR Note/77-35 (1977) + addendum.

10) C. Metzger, Système d'acquisition de données pour Beamscope, CERN/PS/BR Note/77-25 (1977).

11) C. Baribaud et al., Dispositifs de saisie et de traitement des données de mesures du CPS à l'aide d'un ordinateur PDP 11/45, CERN/PS/BR Note/78-13 (1978).

12) K. Schindl, IEEE Trans. Nucl. Sci. NS-26, 3562 (1979).

13) C. Bovet, R. Gouiran, I. Gumowski and K.H. Reich, A selection of formulae and data useful for the design of AG synchrotrons, CERN/MPS-SI/Int. DL/70/4 (1970).

14) C. Bovet, BOOM: Un programme pour l'optique du PSB, SI/Note DL/69/17 (1969). A. Saviolakis, BIGBOOM: An extended version of the program BOOM incorporating a closed-orbit correction option, PS/BR Note/76-27 (1976).

15) F. Schäff, Field distortions by eddy currents in metallic vacuum chambers of the PSB 800 MeV C.O. deflectors, SI/Note MAE/69-11 (1969).

16) M. Perrin, private communication.

17)   M. Chanel, private communication.

18)   Technical specification for the dipole magnets of the 800 MeV Booster-
        Synchrotron (PSB), CERN/SI/Int. MAE/70-2 (1970).
        Spécification pour la fabrication des bobines pour les dipôles du PSB,
        CERN/SI/Int. MAE/70-4 (1970).
        Spécification pour la fabrication des culasses pour les dipôles du PSB,
        CERN/SI/Int. MAE/70-5 (1970).
        Spécification pour les supports des dipôles du PSB, CERN/SI/Int. MAE/70-6
        (1970).

19)   S. Battisti et W. Heinze, Layout détaillé de l'interface de contrôle:
        systèmes de mesure du faisceau PSB (BMS), CERN/PS/CO/Note 79-20 (1979).

20)   C. Carter et al., PS-BR Note in preparation.

21)   H. Schönauer, The Beamscope aperture: choice and consequences for irradia-
        tion, BR Note in preparation.

22)   V. Agoritsas et al., PSB beam observation and measurements, PS/BR/CO/EI/MU/OP
        79-22 (1979).

23)   H. Schönauer, Beamscope - Instructions for use, unpublished operating instruc-
        tion.

24)   P. van der Vossen, Preliminary TEMP-BMC USER Information, unpublished note,
        Sept. 1978.

25)   J.P. Delahaye et al., Shaping of proton distribution for raising the space-
        charge of the CERN PS Booster, 11th Int. Conf. on High-Energy Accelerators,
        CERN, Geneva, 1980 (Birkhäuser Verlag, Basle, 1980), p. 299.

26)   H. Ishimaru et al., Beam size measurement of 12 GeV accelerator by fast
        rotary scraper, IEEE Trans. Nucl. Sci. NS-26, 3358 (1979).

27)   P. Lefèvre, Mesure très peu destructive des distributions transversales dans
        le PS de 800 MeV à 26 GeV, PS/DL/Note 78-8 (1978); and several PS MD News
        by J.P. Bovigny, E. Marcarini, Ch. Steinbeck and M. Van Rooij.

28)   A. Barisy et al., A transverse beam profile monitor for p-p̄ studies in the
        CERN SPS, IEEE Trans. Nucl. Sci. NS-28, 2180 (1981).

BEAM CURRENT TRANSFORMER

DIPOLE

DIPOLE

PRECISION APERTURE RESTRICTION

UNPERTURBED CLOSED ORBIT

DIPOLE

DIPOLE

MPX 4 RINGS 2 PLANES

$\frac{dI}{dT}$

$\frac{dI}{dT}$

DIPOLE SHUNT SIGNAL $\propto I_{dipole}$

BUMP. SUPP.

SHUNT

TRIGGER
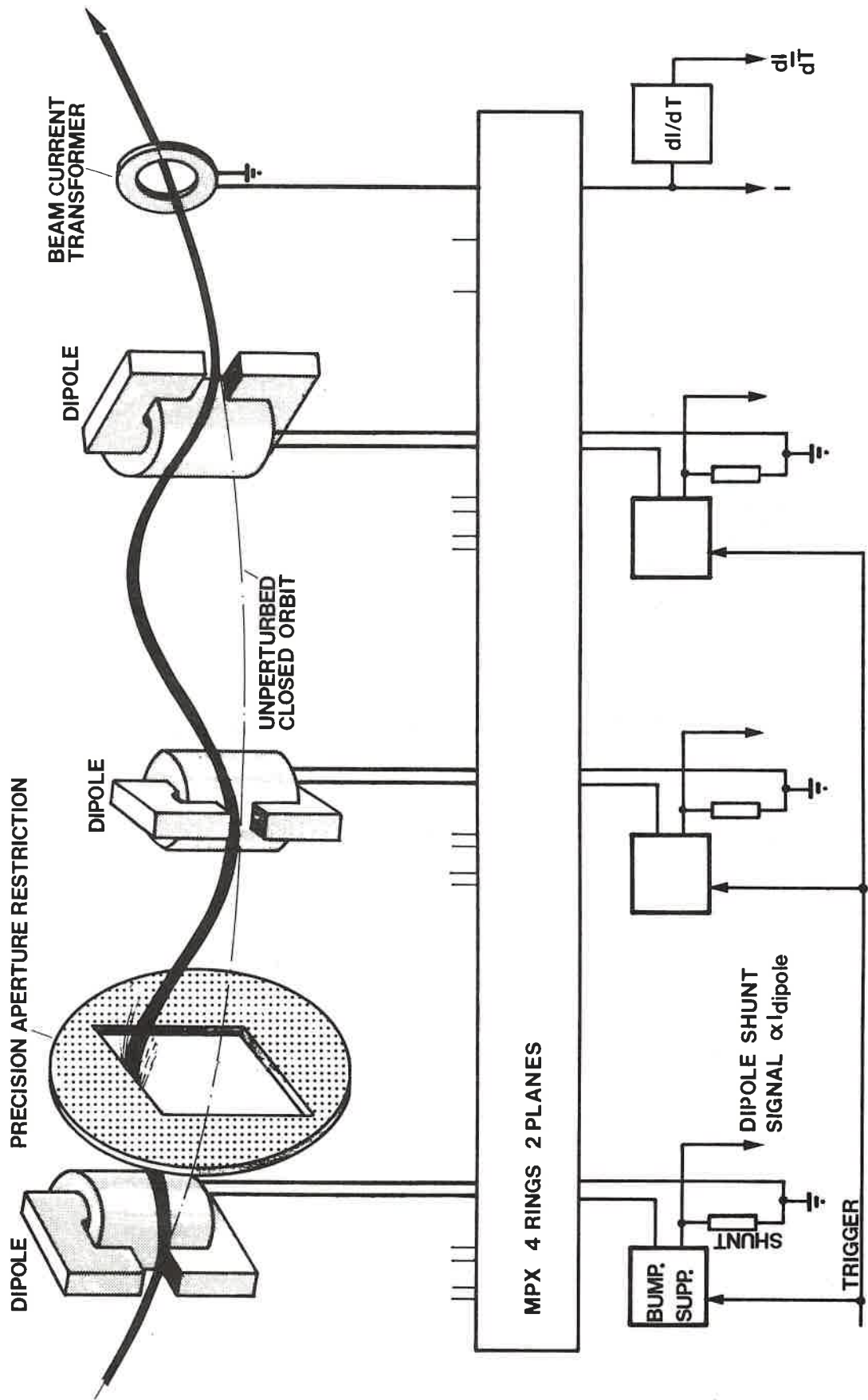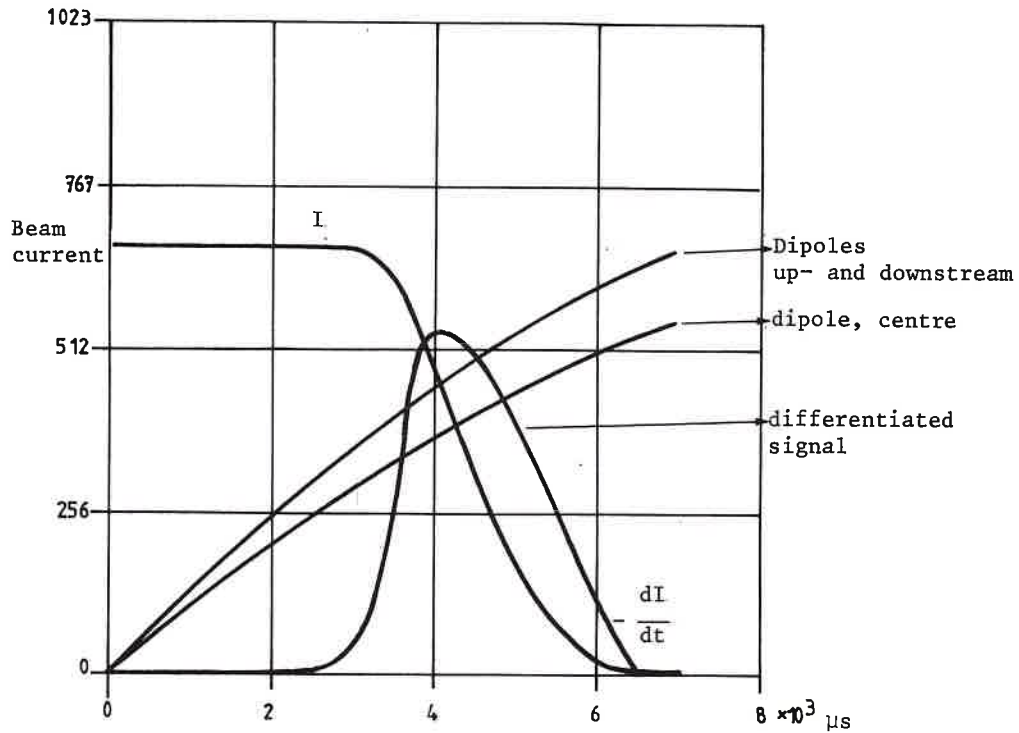
Fig. 2 The five "raw" Beamscope signals (the shunt signals of the two outer dipoles appear as one single trace).
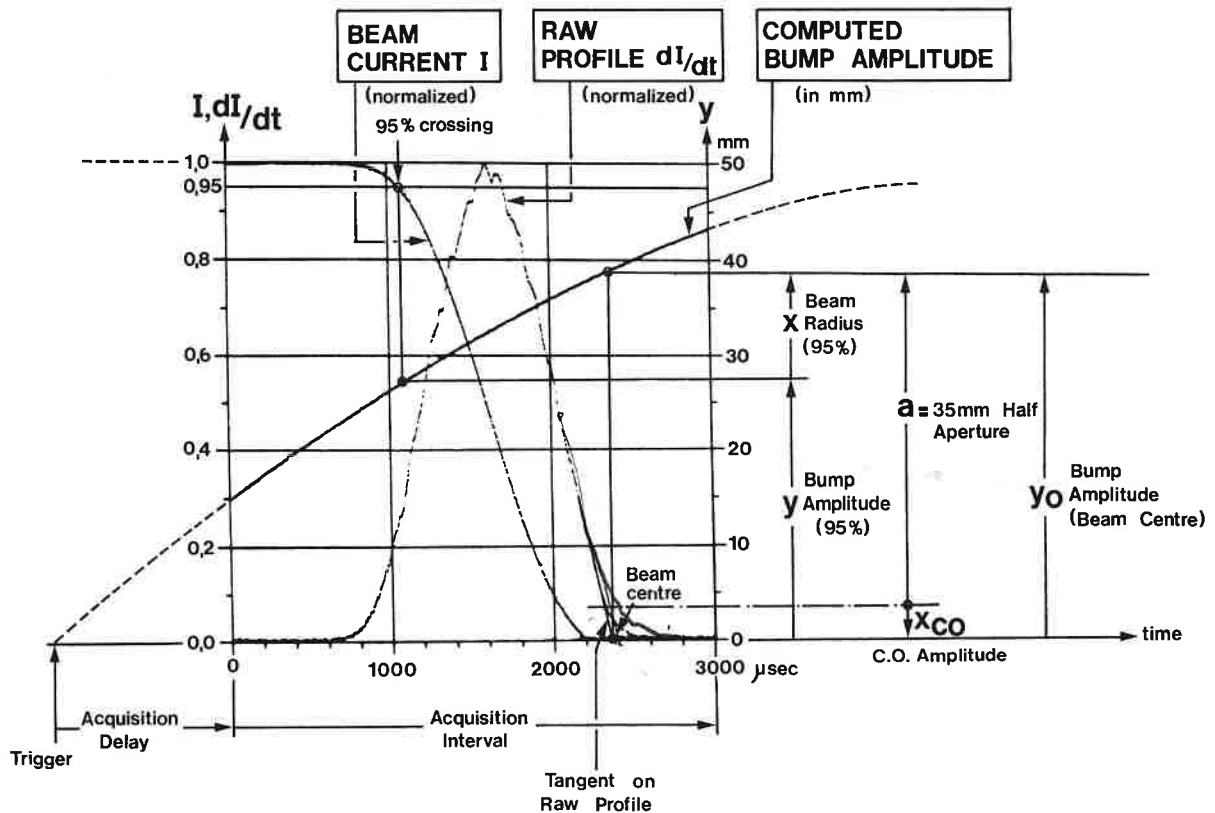
Fig. 3 The three basic Beamscope signals and their interpretation.

APERTURE

DIPOLE

Polarity 1

unperturbed C.O.

Polarity 2

$x_1(95\%)$
$y_1(95\%)$

a

x_{co}

a
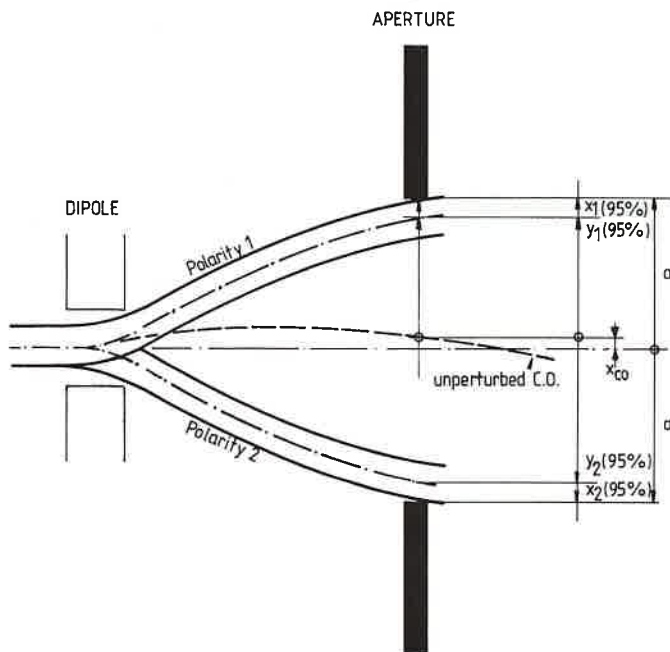
$y_2(95\%)$
$x_2(95\%)$

$$a = x_{co} + y_1(95) + x_1(95)$$

$$a = -x_{co} + y_2(95) + x_2(95)$$

$$2a = y_1(95) + y_2(95) + x_1(95) + x_2(95)$$

$$x = \frac{x_1(95) + x_2(95)}{2} = \bar{x}$$

$$= a - \frac{y_1(95) + y_2(95)}{2}$$

Fig. 4   Principle of the double-pulse method.

BETATRON AMPLITUDE

BETATRON AMPLITUDE
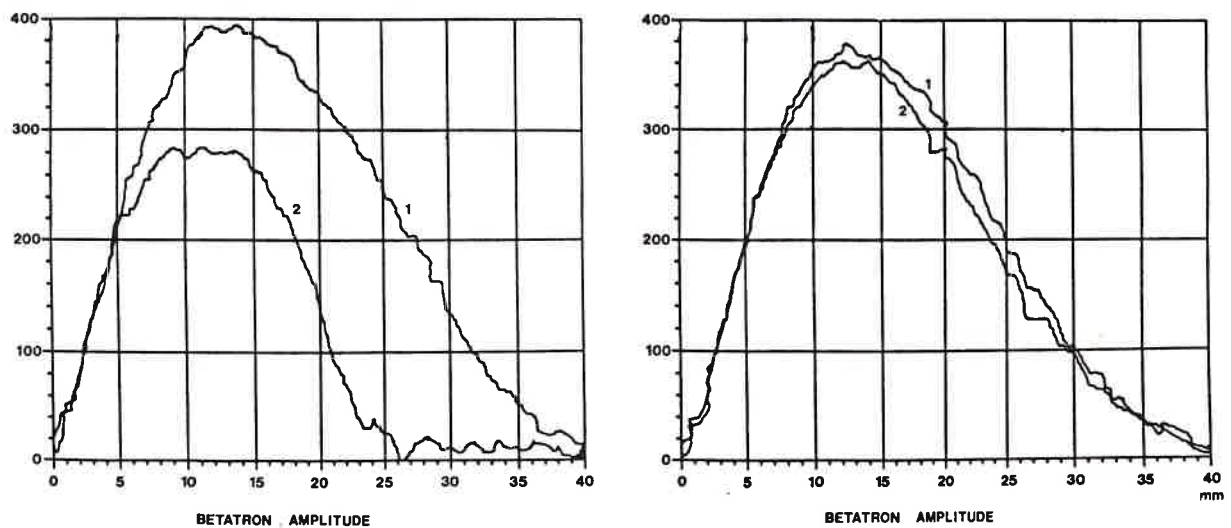
Fig. 5   Effective compensation of a systematic third-order resonance: profiles prior to (1) and after (2) resonance crossing, uncompensated (left) and compensated (right).
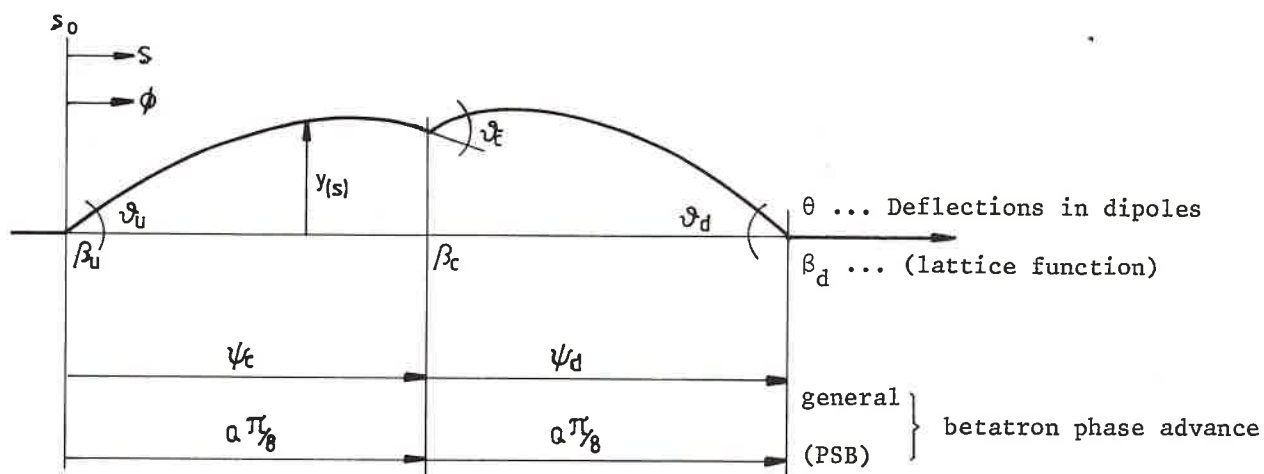
Fig. 6   Nomenclature for computation of bump amplitude.

$$x = nd$$

$$\cos \phi_n = \frac{r-x}{r}$$

$$\phi_n = \arccos \left(1 - \frac{x}{r} \right)$$
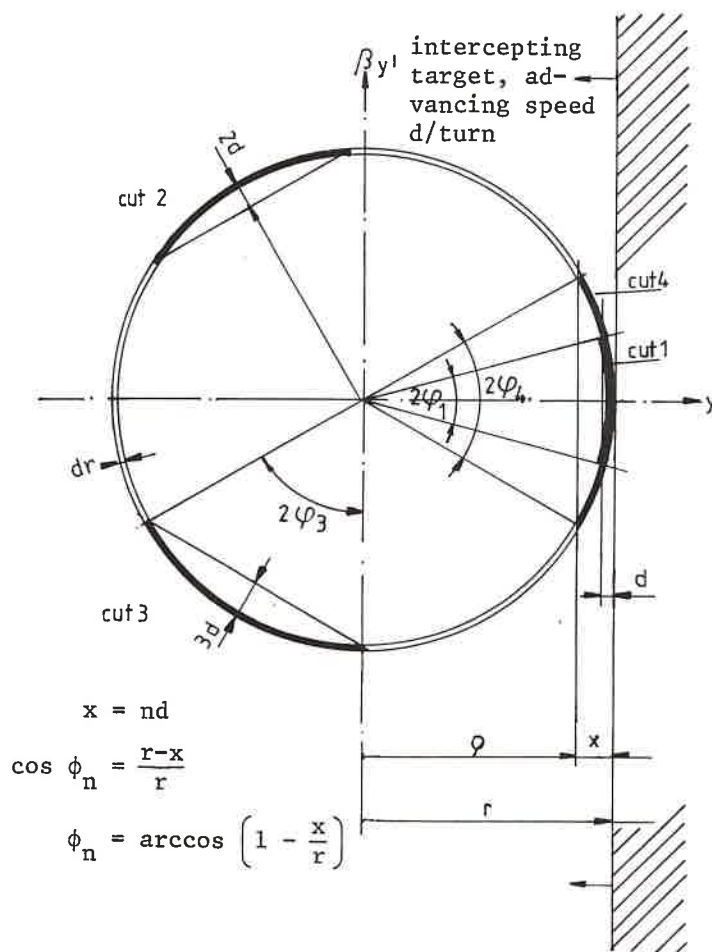
Fig. 7   Successive interception of particles of betatron amplitude r (for a fractional part of the Q-value q = $^1/_3$).
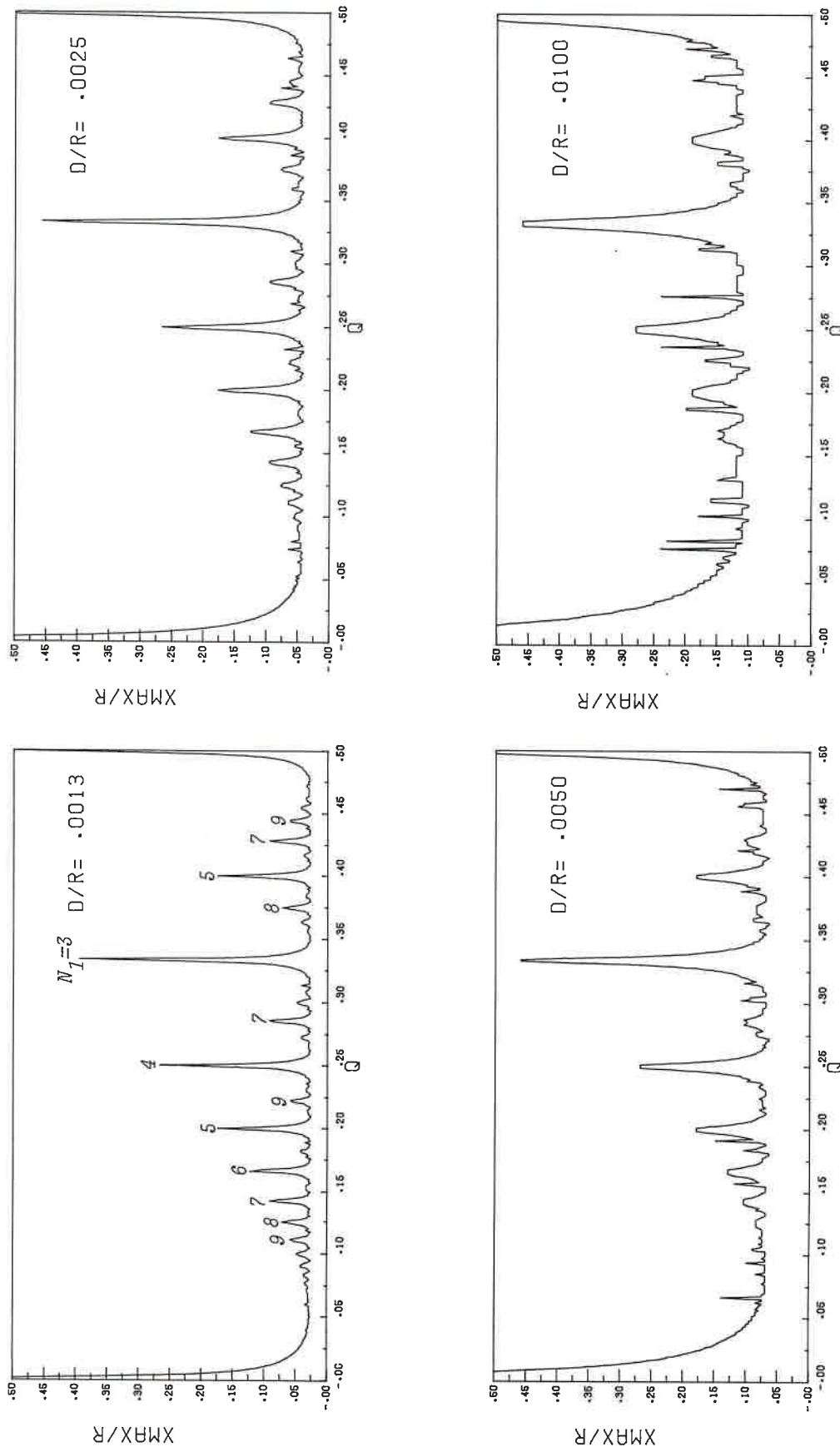
Fig. 8 Normalized width x_{max}/r of the resolution function as a function of q (fractional part of tune Q) for different scraping speeds d/r, calculated for 95% particles intercepted. Numbers labelling the peaks indicate the order of the resonances.
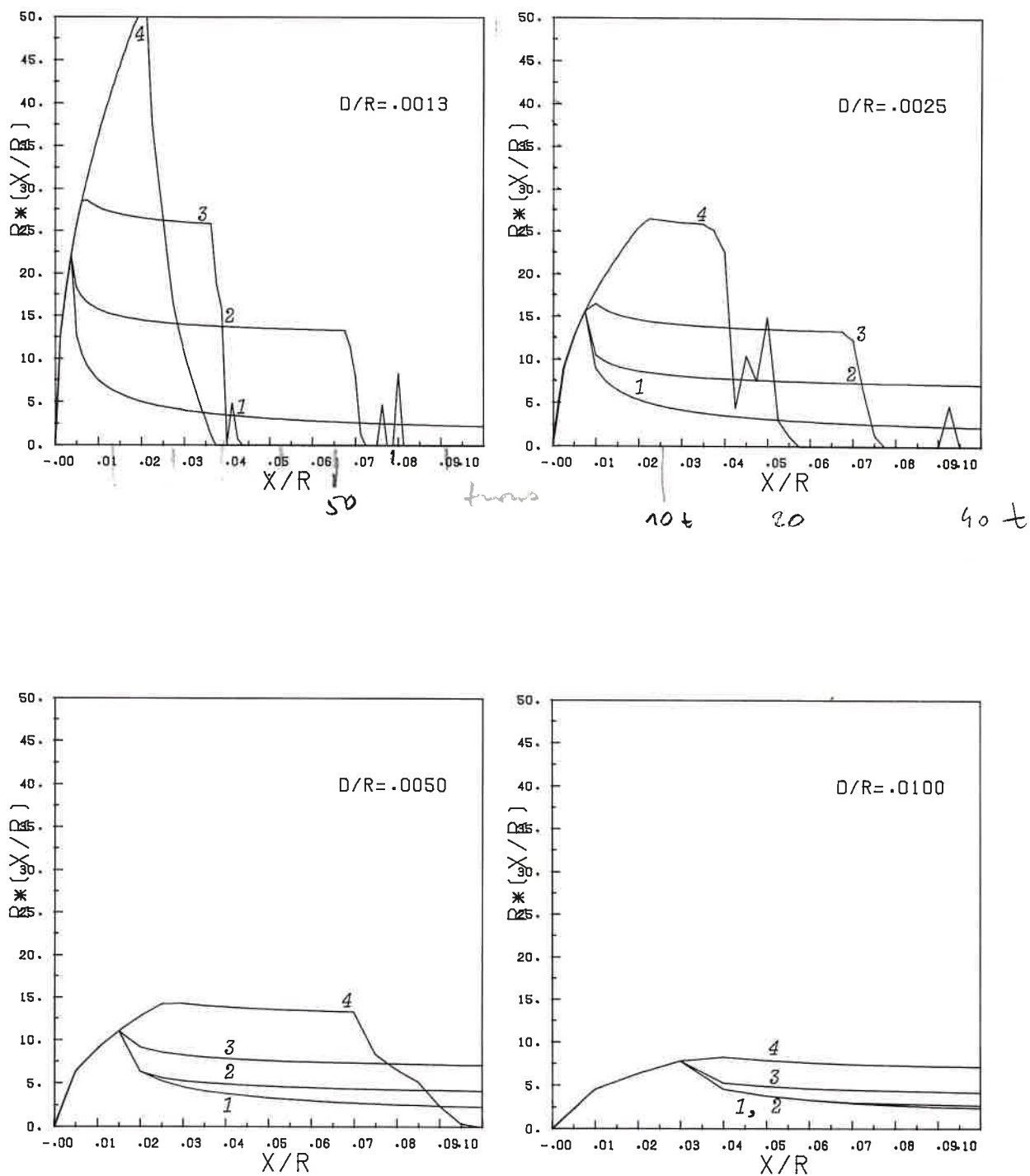
Fig. 9 Normalized resolution function for various q values showing the effect of approaching a resonance q = $\frac{1}{3}$ + δ, for four scraping speeds d/r. Curves 1, 2, 3, 4 show δ = 0, 0.005, 0.01, and 0.02, respectively.
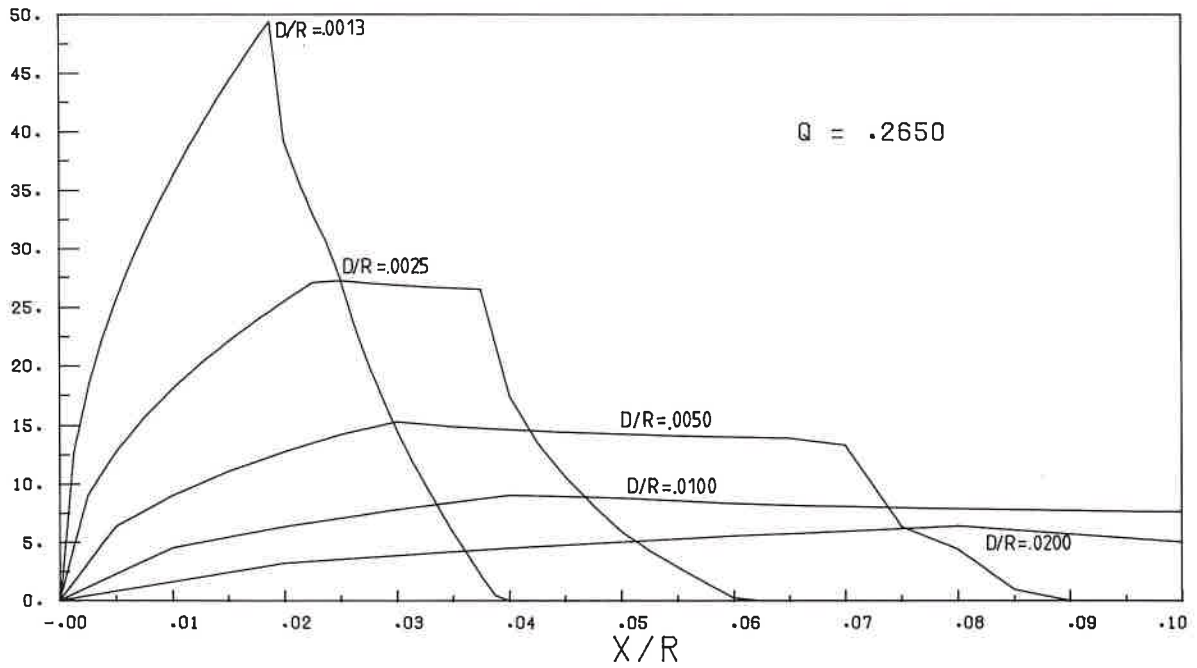
Fig. 10 Normalized resolution function R*(x/r) = r R(r,x) far from a resonance: influence of scraping speed d/r.
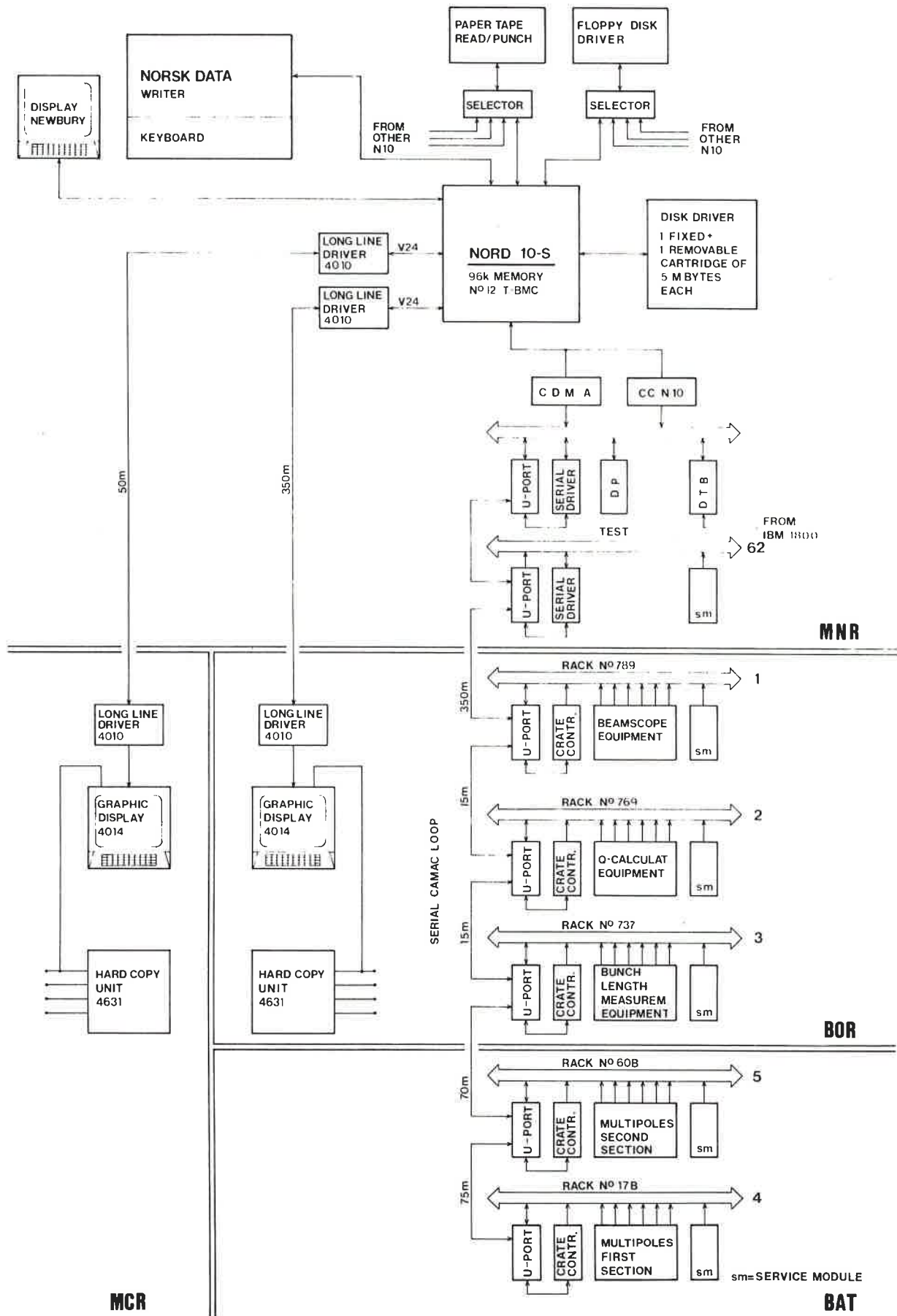
Fig. 11 Layout of the Temporary Beam Measurement Computer and its CAMAC loop.
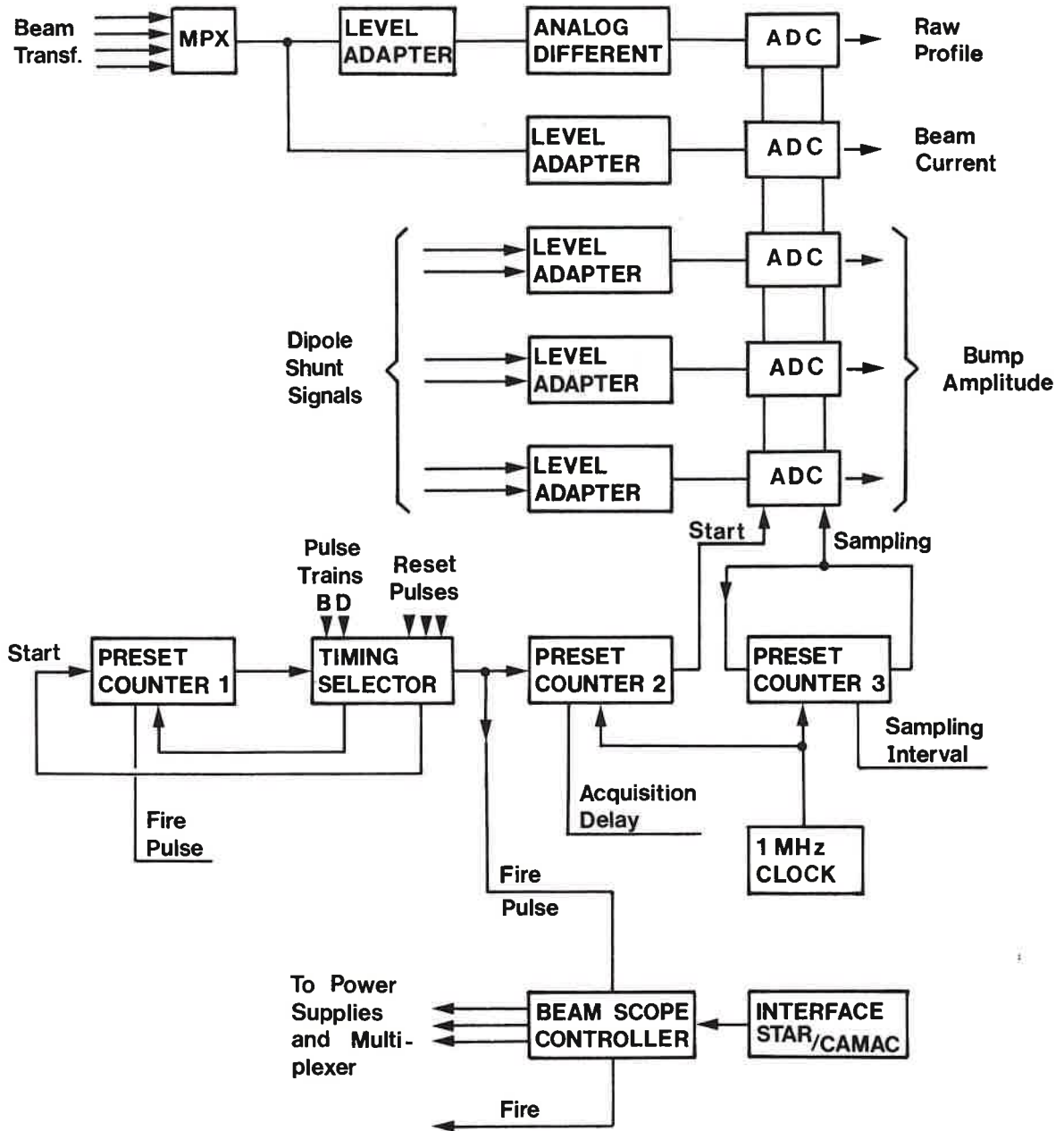
Fig. 12 Functional configuration of Beamscope CAMAC crate.

	Multiplexer AMX 16/1	High Speed Digitizer SA/D 1001	High Speed Digitizer SA/D 1001	Dual Level Adaptor (Home made)	High Speed Digitizer SA/D 1001	High Speed Digitizer SA/D 1001	Dual Level Adaptor (Home made)	High Speed Digitizer SA/D 1001	Dual level Adaptor (Home made)	Timing and IPL	Selector (Home made)		Dual Preset Counter PS 2002	Dual Preset Counter PS 2002		Differentiator (Home made)		Data way Service Module JDS 10					U-Port Adaptor K-3932		Serial Crate Controller K-3952
1	2	3	4	5	6	7	8	9	10	11	12	13	14	15	16	17	18	19	20	21	22	23	24	25

Fig. 13 Physical configuration of Beamscope CAMAC crate.

BEAMSCOPE EMITTANCES 26/ 4/1979   8:35
D 150 FROM FTR   IPL 1
RING P/P HOR. EMITTANCE   VERT. EMITTANCE
     E10 PHYSICAL(NORM)   PHYSICAL (NORM)

1	514	34.3 (53.4)	21.5 (33.6)
2	464	34.4 (53.7)	18.1 (28.3)
3	568	30.3 (47.2)	18.1 (28.2)
4	548	28.7 (44.7)	18.6 (29.1)

AMPLITUDE PROFILES

H

Fig. 15 Standard Beamscope output.
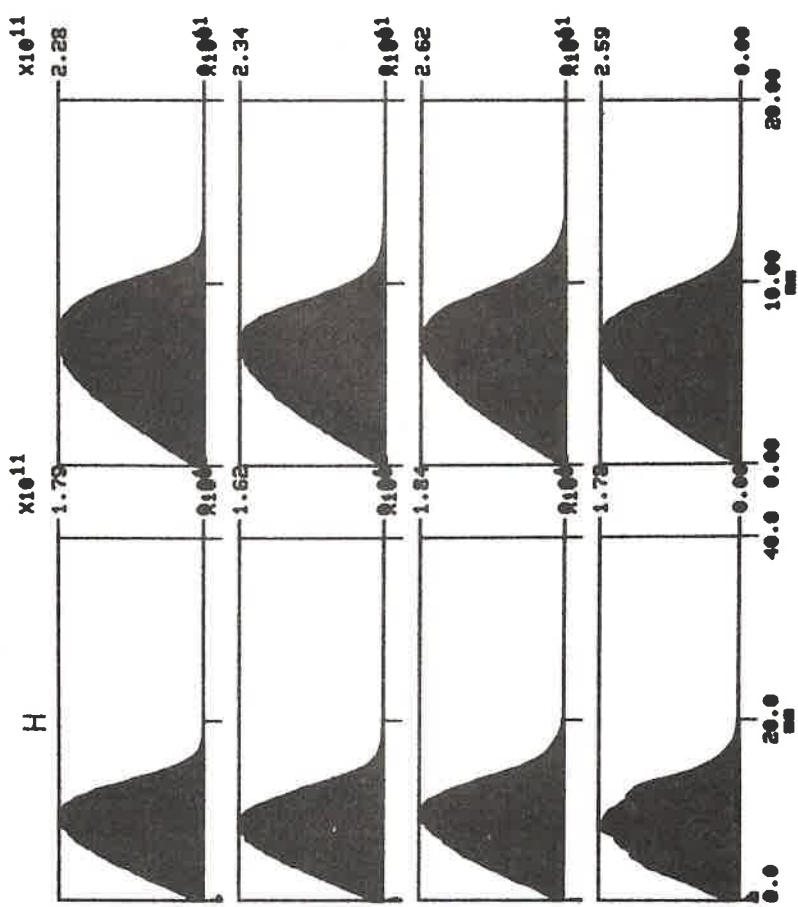
BEAMSCOPE VERS. 6.01 *   EJECTION FILE *

CHOOSE YOUR PROGRAM:

OPERATION PROGRAMS
EMITTANCE MEASUREMENT, 1 RING   (1,2,3 OR 4)
EMITTANCE MEASUREMENT, ALL RINGS   (5)
EMITTANCES FOR AA, RINGS 2 + 3   (6)
                        1 + 4   (7)

PROGRAMS FOR MACHINE EXPERIMENTS
SET MEASURMT PARAMETERS   (11)
COARSE AMPLITUDE PROFILE(S)   (12)
CALIBRATED AMPLITUDE PROFILE(S)   (13)
CALIBRATED EMITTANCE PROFILE(S)   (14)
2-DIM. DISTRIBUTION INITIALISATION   (15)
2-DIM. AMPLITUDE DISTRIBUTION   (16)
2-DIM. EMITTANCE DISTRIBUTION   (17)

UTILITIES AND TEST PROGRAMS
SET PROCESS PARAMETERS (SCOPE)   (21)
SET PROCESS PARAMETERS (NO SCOPE)   (22)
CHANGE FILE   (23)
COPY IPL   (24)
SET SOFTWARE PARAMETERS   (25)
STATISTICS FOR BAD PULSE REJECT   (26)
SET POLARITY   (27)
AUTOSCOPE   (28)
LIBRARY PROGRAM   (30)

EMITTANCE MEASUREMENT/ TARGET COMPARISON
ONE POLARITY, FULL SCRAPING   (31)
ONE POLARITY, 5x SCRAPING   (32)
ALT.POLARITY, FULL SCRAPING   (33)
ALT.POLARITY, 5x SCRAPING   (34)
LIBRARY PROGRAM   (40)

EXIT FROM PROGRAM   (999)

TYPE PROGRAM NUMBER :

Fig. 14 The "menu" of Beamscope subprograms.

Fig. 16 Axonometric display of a series of normalized amplitude profiles.

Fig. 17 Output of one of the detailed emittance measurement programs (No. 33 of the menu of Fig. 14), giving beam radius and emittance of the computed closed-orbit amplitude and the "reconstructed aperture" and its error. If a comparison target measurement was made and input, relative emittance and absolute beam radius error would be computed too.
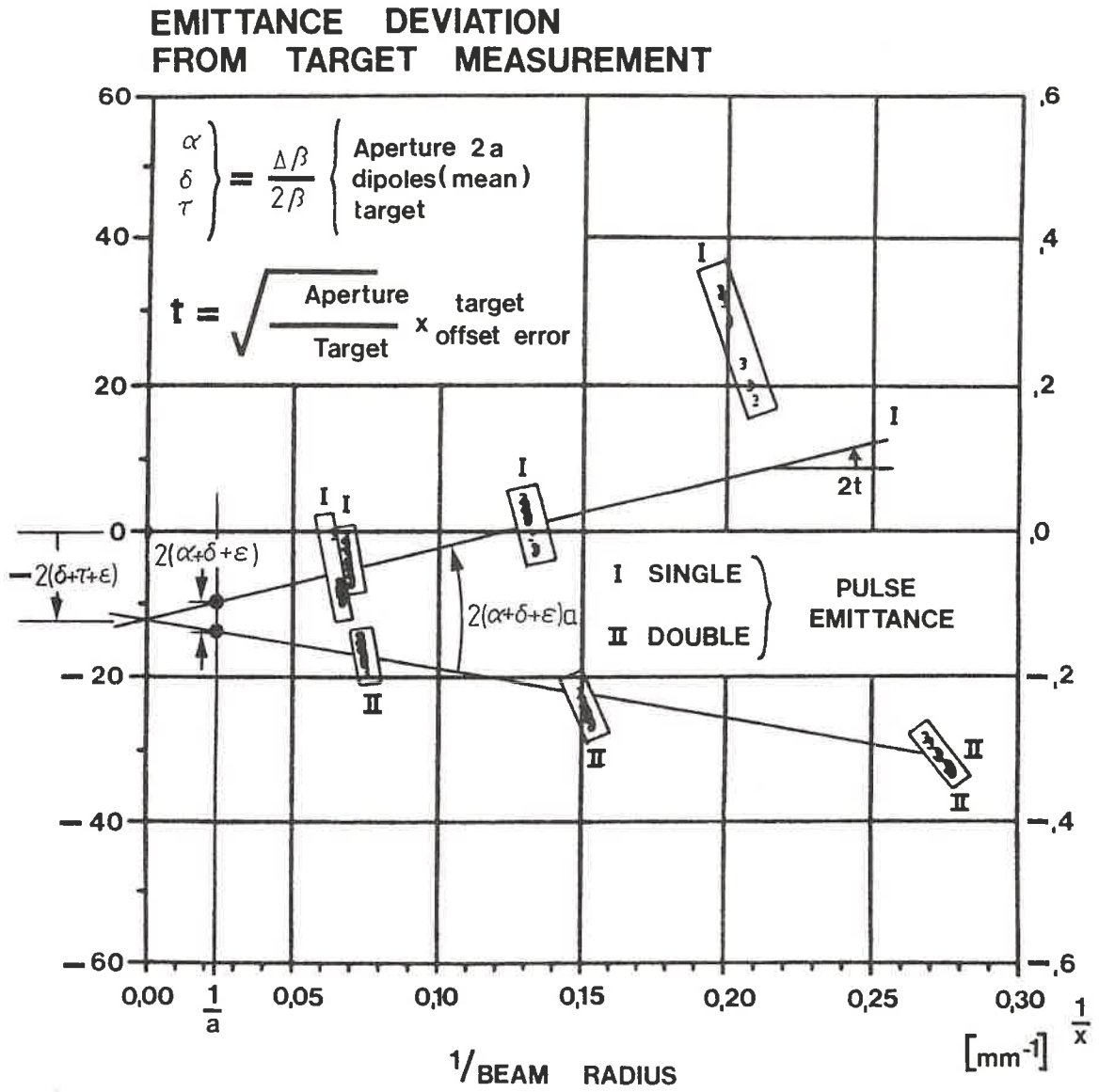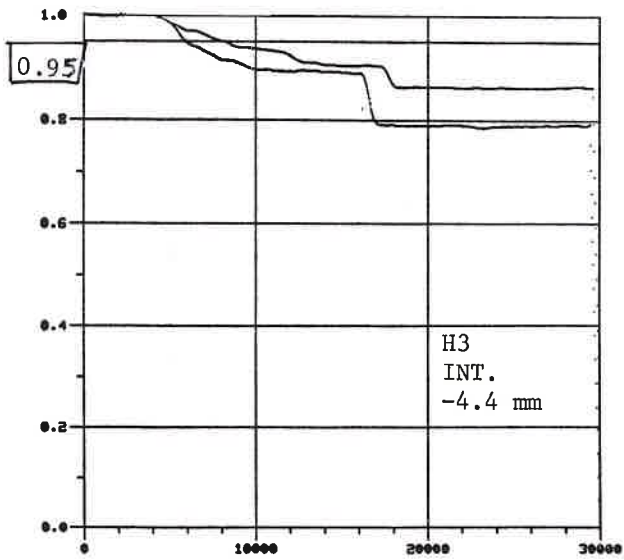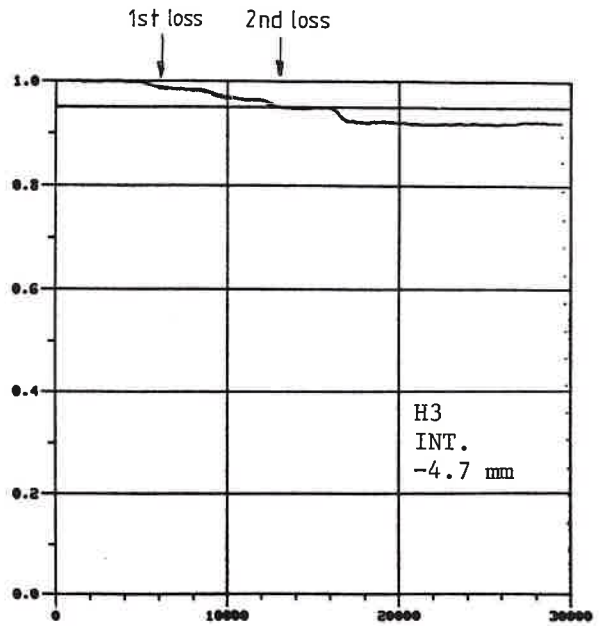
Fig. 18 Scatter plot of Beamscope versus target comparison measurements: plot of $\Delta\varepsilon/\varepsilon$ versus $1/x$.

1st loss = 5%   2nd loss = 5%

1st loss   2nd loss

H3
INT.
-4.4 mm

H3
INT.
-4.7 mm

Note the jitter between two
consecutive pulses

V3
BOTTOM
-9.1 mm

V3
BOTTOM
-9.6 mm

μs   μs
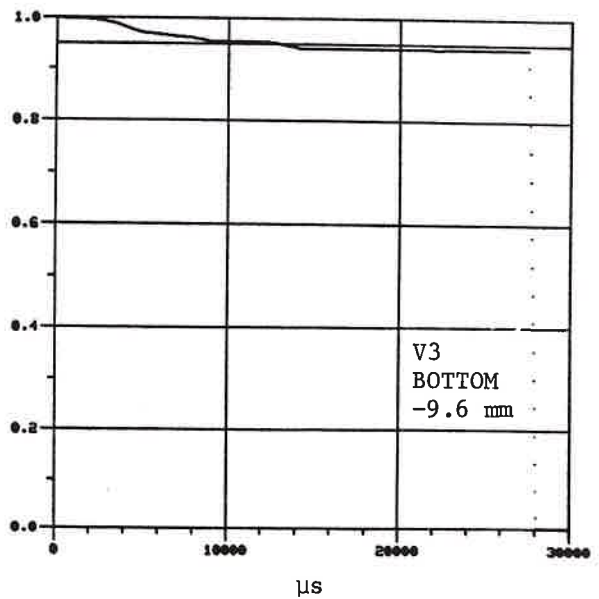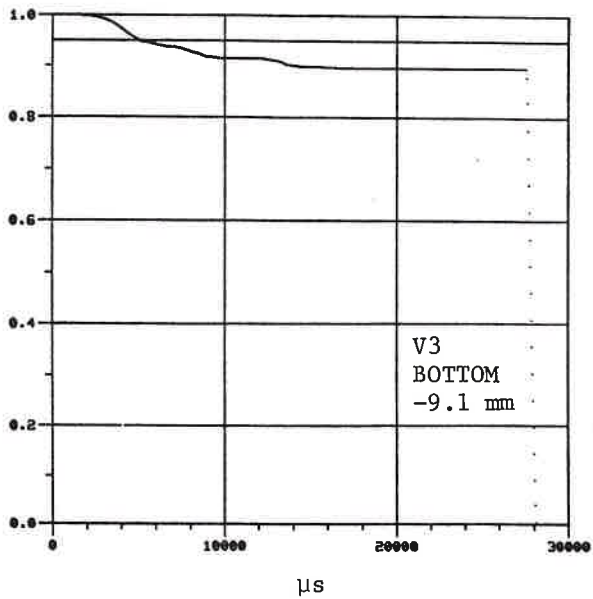
Fig. 19 Beam loss patterns due to target measurements: interpretations of "5% loss".

Horizontal   Vertical
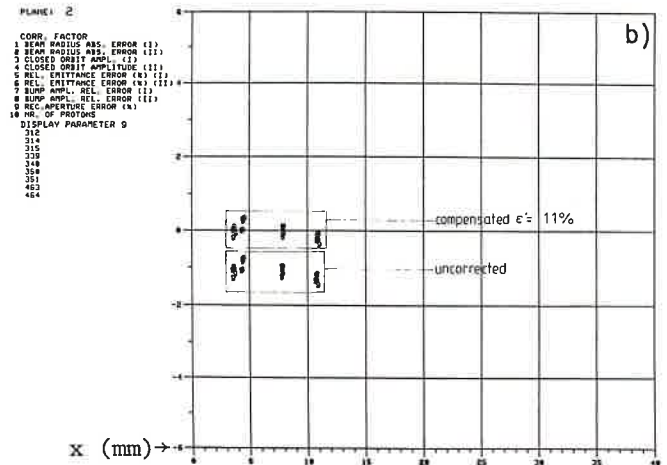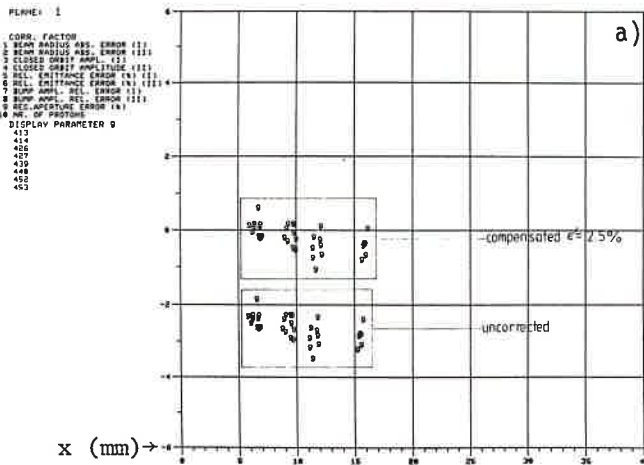
Relative error in "reconstructed aperture", uncorrected (a) and after compensation
by deliberate calibration "error" ε' (b).
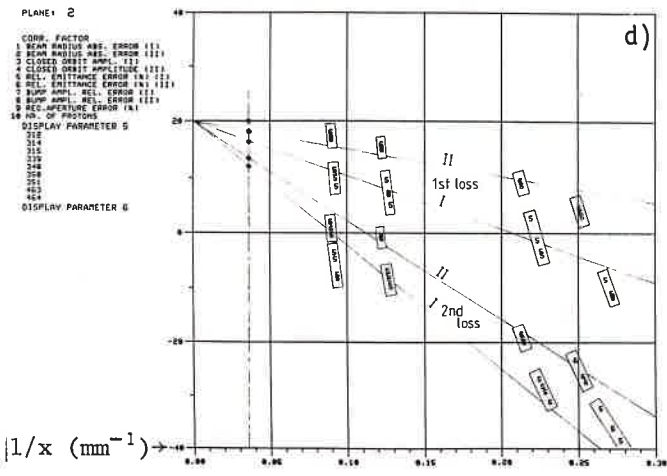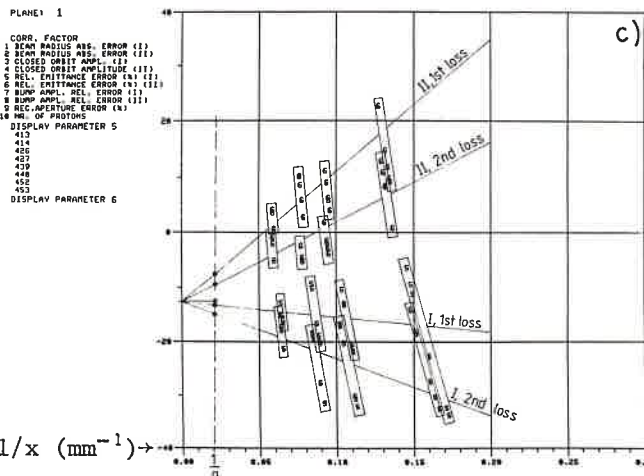
Relative emittance error, uncorrected, vs. 1/beam radius for single-pulse (I) and
double-pulse (II) method, for two interpretations of target measurements: first (c)
or second (d) loss being significant.
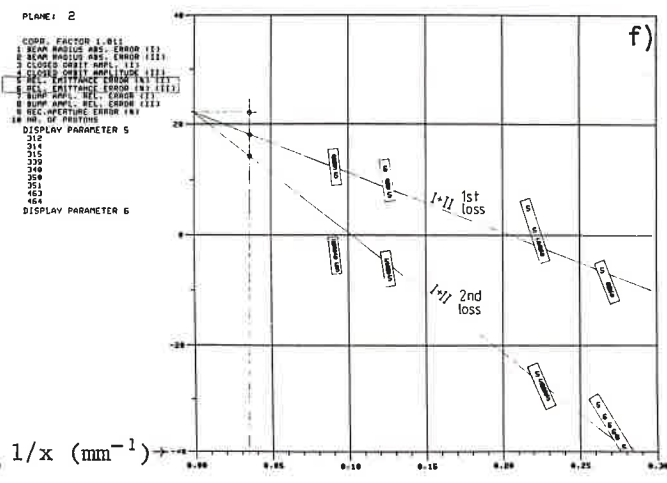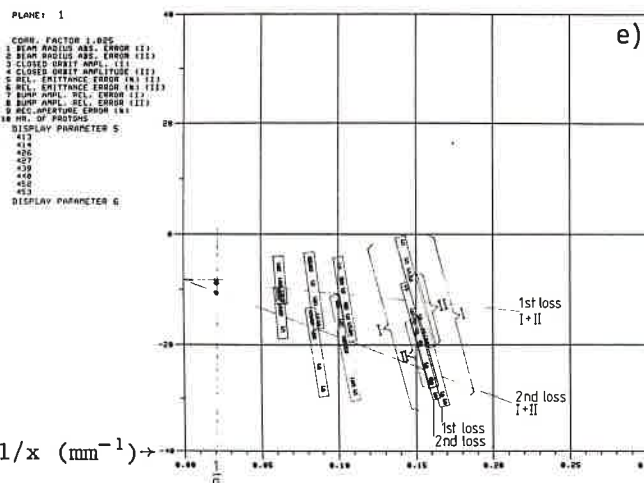
As above, taking first (e) and second (f) loss as significant, after corrections
as found from (a) and (b). Single- and double-pulse measurements now coincide.

Fig. 20 Results of comparison measurements Beamscope versus targets for Ring 3.
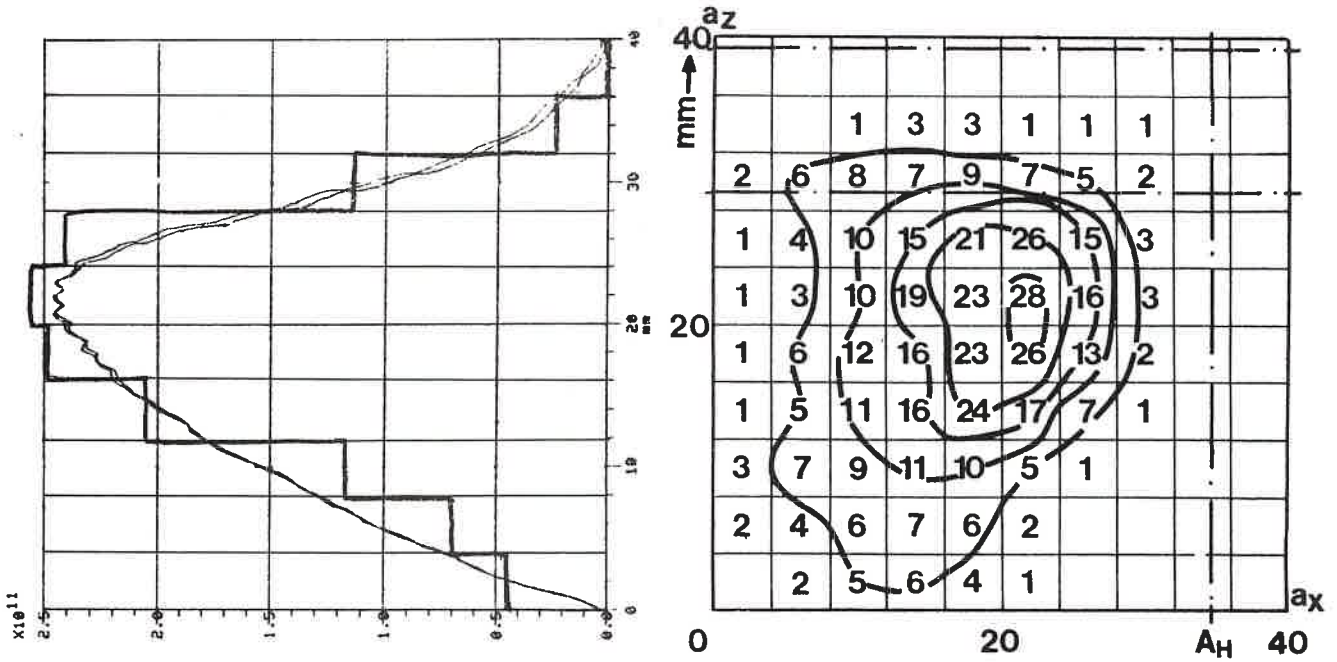
Fig. 21 Two-dimensional amplitude distribution (in 10^{10} p per cell) derived from a series of 10 horizontal Beamscope profiles with 10 different positrons of the vertical target. Left: comparison of the vertical projection histogram of the matrix with a vertical Beamscope profile.
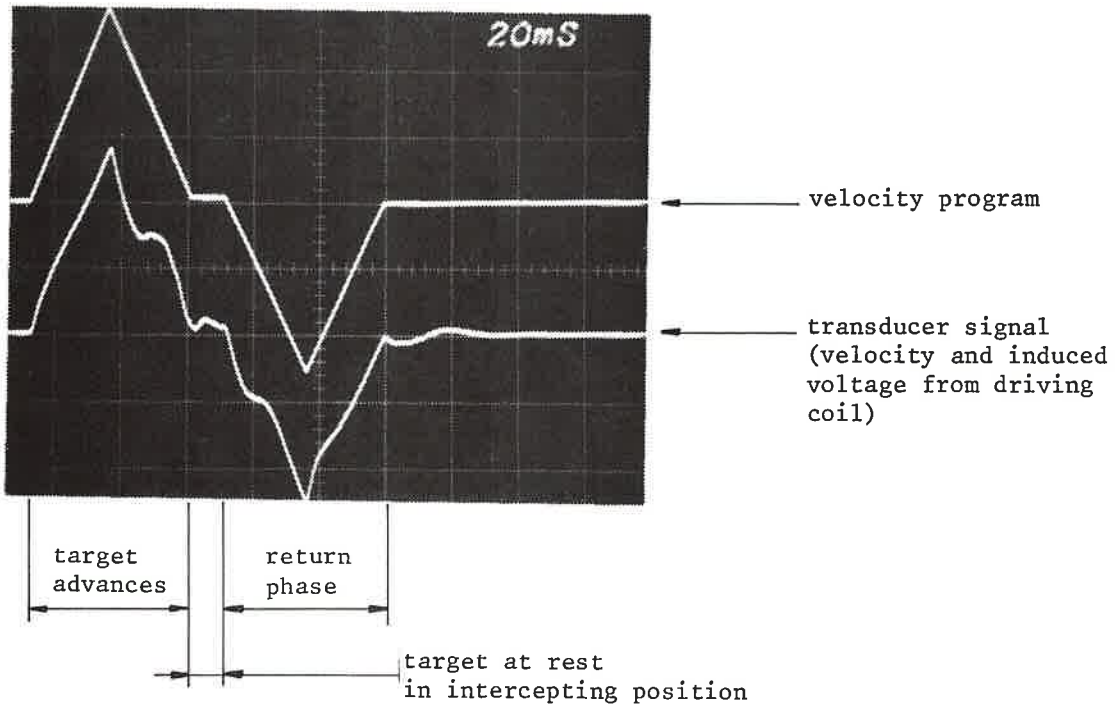

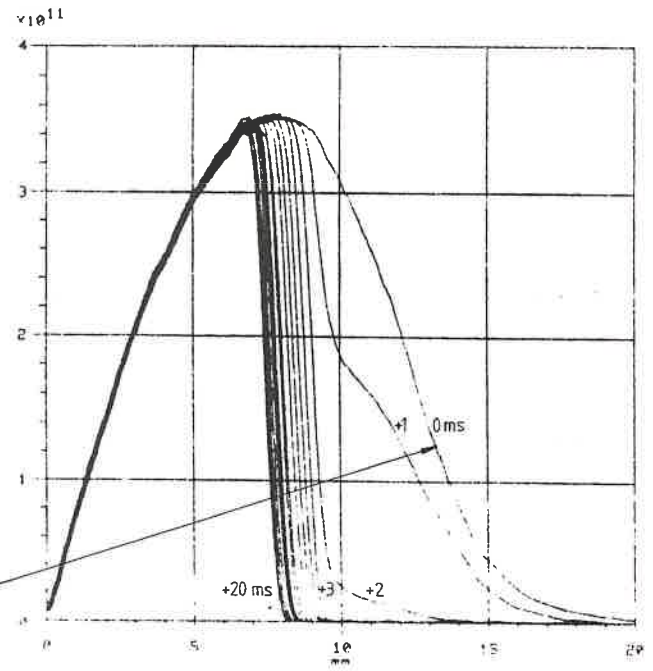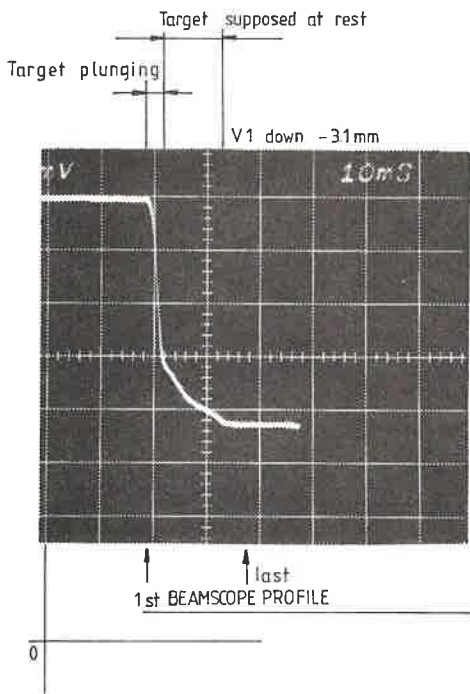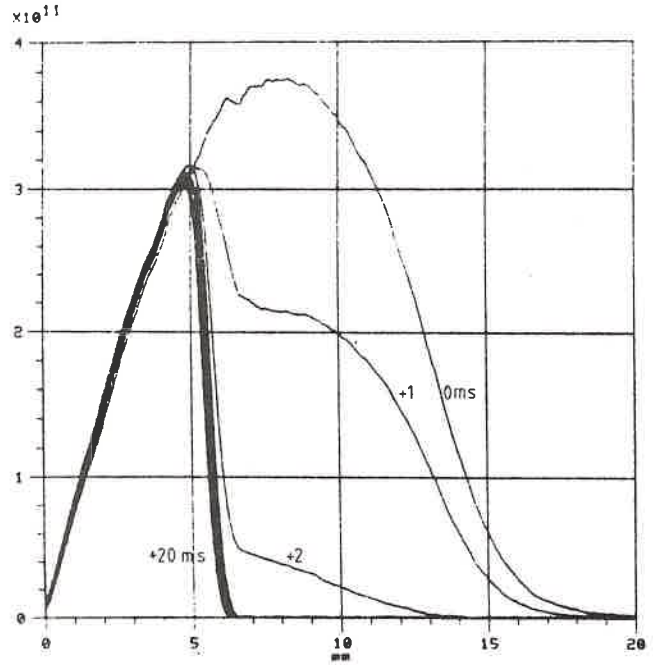Fig. 22 Reference signals in velocity program of PSB Measurement Targets.
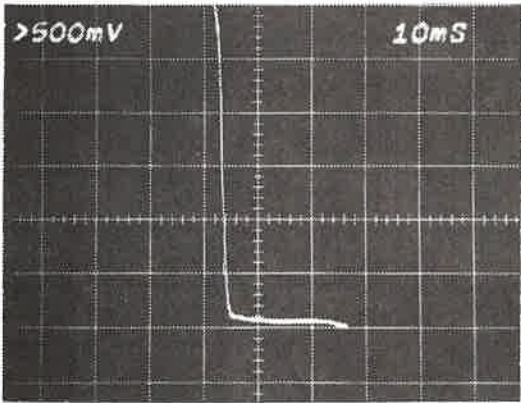
Fig.   Beamscope profile series showing a) correct and b) faulty behaviour of a plunging target. In (b) the target continues to penetrate slowly into the beam, causing slow loss which is visible on the beam current signal (left). In (a) the target stays quiet once plunged and there is no beam loss during this phase. Time increment: 1 ms between Beamscope profiles.
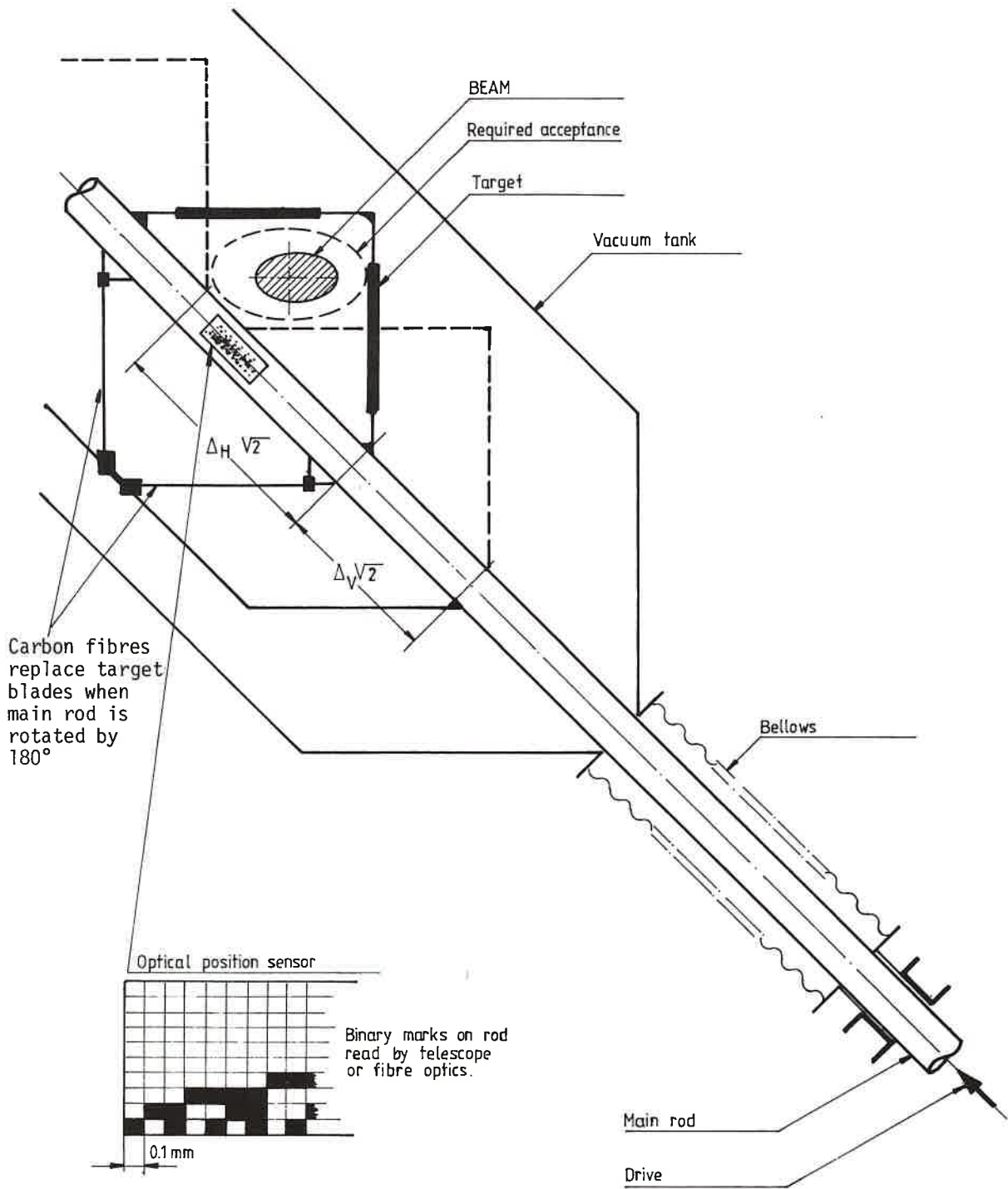
Fig. 24 Basic principle of a General Target Device.

Appendix

The Resolution Function $R(r,\rho)$ of a measurement device links the observed response $x(r)$ to the true response $t(r)$:

$$x(r) = \int R(r,\rho)\, t(\rho)\, d\rho\ , \quad \int R(r,\rho)\, d\rho = 1\ .$$

For a sharp (true) response $t(r) = \delta(r-r_0)$, the observed response is the resolution function itself:

$$x(r) = R(r,r_0)\ .$$

Referring to Fig. 7, $R(r,\rho)$ is determined by the arc length of the phase-space trajectory intercepted when the target advances from ρ to $\rho - d\rho$.

The resolution function also depends strongly on the fractional part q of the Q value; in order to describe a beam of a Q spread $G(q)$, one has to compute

$$R(r,\rho) = \int dq\, R(r,\rho;q)G(q)\ , \quad \int G(q)\, dq = 1\ .$$

In the following we compute $R(r,\rho;q)$ only and drop the argument q.

We will make use of the following variables:

q = M/N, the fractional part of Q, assumed to be rational;

q $\simeq M_1/N_1$, the "closest resonance" with small N_1, i.e. $N_1 < 10$;

δ = $\left| q - \dfrac{M_1}{N_1} \right| = \left| \dfrac{M}{N} - \dfrac{M_1}{N_1} \right|$, $\quad \Delta = 2\pi\delta\, \dfrac{r}{d}$;

n, the revolution number from the beginning of interception of amplitude r;

$2\phi_n$ the arc length intercepted during the nth revolution (see Fig. 7):

$$\phi_n = \arccos\left(1 - \frac{nd}{r} \right)\ ;$$

d the target advance per revolution;

x = $r - \rho$, $\quad \xi = \dfrac{x}{r}$, $\quad \eta = \sqrt{1 - \dfrac{\rho^2}{r^2}}$.

The (already normalized) loss per turn depends on the occurrence or not of overlapping cuts. Referring to the cases of overlap as depicted in Fig. A1, we have the expressions

$$\Delta R_n(r) = (1/2\pi) \times$$

$$\begin{cases} 2\phi_n & \text{case (a), no overlap: } n < N_1 \text{ or } \phi_n + \phi_{n-N_1} < 2\pi\delta \\[2mm] \phi_n - \phi_{n-N_1} + 2\pi\delta N_1 & \text{cases (b,c), partial overlap: } \phi_n - \phi_{n-N_1} < 2\pi\delta N_1 < \\ & \hphantom{\text{cases (b,c), partial overlap: }} < \phi_n + \phi_{n-N_1} \\[2mm] 2(\phi_n - \phi_{n-N_1}) & \text{case (d): } 2\pi\delta N_1 < \phi_n - \phi_{n-N_1} \\[2mm] 2(\phi_n - \phi_{n-N}) & \text{case (e): } n > N \end{cases} \quad \left.\vphantom{\begin{matrix}a\\b\end{matrix}}\right\} \text{ full overlap}$$

The resolution function follows straightforwardly by division through d and with $n = x/d = r - \rho/d$:

$$R(r,\rho) = \frac{1}{2\pi d} \begin{cases} 2\phi(x) & \text{(a)} \\ \phi(x) - \phi(x-N_1 d) + 2\pi\delta N_1 & \text{(b,c)} \\ 2\left[\phi(x) - \phi(x-N_1 d)\right] & \text{(d)} \\ 2\left[\phi(x) - \phi(x-Nd)\right] & \text{(e)} \end{cases}$$

$$\phi(x) = \arccos\left(1 - \frac{x}{r}\right)$$

$$\phi(x) - \phi(x-N_1 d) \cong N_1 d \frac{d\phi(x)}{dx}.$$

$R(r,\rho)$ is different from zero only for $\rho_{min} < \rho < r$; ρ_{min} is determined by the condition that the whole arc 2π is scraped off:

$$\int_{\rho_{min}}^{r} R(r,\rho)\, d\rho = 1 \qquad \text{or} \qquad \int_{0}^{x_{max}} R(r,x)\, dx = 1$$

For δ sufficiently large, one can assume that there is no overlap, or very little, until the whole arc is intercepted. In this case ρ_{min} is solely determined by expression (a):

$$\frac{2}{2\pi d} \int_{\rho_{min}}^{r} \arccos \frac{\rho}{r}\, d\rho = \frac{r}{\pi d}\left[\eta - \sqrt{1-\eta^2}\, \arcsin \eta\right] = 1$$

$$\eta^2 = 1 - \left(\frac{\rho_{min}}{r}\right)^2 \cong \frac{2x_{max}}{r}.$$

The square bracket can be approximated by

$$[\quad] \cong \frac{\eta^3}{3} \cong \frac{1}{3}\left(\frac{2x_{max}}{r}\right)^{3/2},$$

$$\frac{x_{max}}{r} \cong \frac{1}{2}\left(3\pi\frac{d}{r}\right)^{2/3}.$$

In order to check the range of validity of this expression, we compute x_1, the cross-over value between cases (a) and (b,c):

$$\phi(x_1) + \phi(x_1-N_1 d) \leq 2\pi\delta N_1,$$

or

$$2\phi(x_1-N_1 d/2) \cong 2\pi\delta N_1$$

$$\arcsin y_1 \cong y_1 \cong \pi\delta N_1$$

$$y_1^2 = 1 - \frac{(\rho_1 + N_1 d/2)^2}{r^2} \simeq \frac{2x_1 + N_1 d}{r} \simeq \pi^2\delta^2 N_1^2$$

$$\frac{x_1}{r} \simeq \frac{\pi^2 N_1^2 \delta^2}{2} - \frac{N_1 d}{2r}$$

$$2\pi\delta N_1 = \phi(x_1) + \phi(x_1 - N_1 d) \simeq \arccos\left(1 - \frac{x_1}{r}\right) \simeq \sqrt{\frac{2x_1}{r}} \quad \text{for small } \frac{x_1}{r} .$$

Comparing x_1 and x_{max} we obtain an inequality for δ giving the condition for essentially non-overlapping scraping:

$$\frac{x_{max}}{r} = \frac{x_1}{r} = \frac{1}{2}\left(3\pi\frac{d}{r}\right)^{2/3} \simeq \frac{1}{2}\,\pi^2 N_1^2 \delta^2 \quad,$$

$$\delta > \delta_1 = \frac{\left(3\pi\frac{d}{r}\right)^{1/3}}{\pi N_1} .$$

Another cross-over $x_2(\delta)$ between cases (b,c) and (d) of Fig. A1, i.e. between partial and full overlapping, is important. We obtain it from the condition (see Fig. A1)

$$2\pi N_1 \delta = \phi_{n_2} - \phi_{n_2 - N_1} = \arccos\frac{\rho^2}{r} - \arccos\frac{\rho^2 + N_1 d}{r}$$

$$= \frac{N_1 d}{r}\left(1 - \frac{\rho_2^2}{r^2}\right)^{-\frac{1}{2}} = \frac{N_1 d}{T\eta_2}$$

$$\eta_2 = d/(2\pi\delta r) = \frac{1}{\Delta} \simeq \sqrt{2x_2/r} .$$

Plotting $\delta(x_1)$ and $\delta(x_2)$ in a δ versus x/r diagram (Fig. A2), these curves separate the different regimes of overlapping; when computing $R(r,\rho)$ and x_{max}, one notices that one has to distinguish five cases (I)-(V) of δ.

The (in some cases approximate) expressions for $R(r,x)$ are compiled below: x_{max} is given only for the limiting cases (I) and (V); the expressions for the intermediate cases are complicated and of little practical interest.

The table on the opposite page gives the normalized resolution function $R^*(x/r) = r\,R(r,x)$ for the various cases, using the following expressions:

$$R_1 = \frac{1}{\pi\theta}\arccos(1 - \xi) \qquad \text{(no overlapping)}$$

$$R_2 = N_1\left[\frac{1}{2\pi\eta} + \frac{\delta}{\theta}\right] \qquad \text{(partial overlapping)}$$

$$R_3 = \frac{N_1}{\pi\eta} \qquad \text{(full overlapping)}$$

$$\xi_1 = \frac{1}{2}(N_1\pi\delta)^2 \quad, \qquad\qquad \delta_1 = \frac{(3\pi\theta)^{1/3}}{\pi N_1} \quad,$$

$$\xi_2 = N_1\theta \quad, \qquad\qquad \delta_2 = \frac{1}{\pi}\left(\frac{2\theta}{N_1}\right)^{\frac{1}{2}}, \;\; \delta_3 = \frac{\delta_2}{4} \quad,$$

$$\xi_3 = \frac{\theta^2}{8\pi^2\delta^2} \quad, \qquad\qquad \delta_4 = \frac{\theta}{2\pi\sqrt{2\left(1-\cos\frac{\pi}{N_1}\right)}} \quad,$$

where

$$\theta = d/r , \quad \xi = x/r ,$$

$$\eta = \sqrt{1 - \left(\frac{\rho}{2}\right)^2} \cong 2\xi .$$

← CORR

Domain		$R^*(\xi) = r\, R(r,x)$	
Notation Fig. A2	Limitations	Expression	Validity
I	$\delta > \delta_1$	R_1	$0 < \xi < \xi_{max} = \tfrac{1}{2}(3\pi\theta)^{2/3}$
II	$\delta_2 < \delta < \delta_1$	R_1	$0 < \xi < \xi_1$
		R_2	$\xi_1 < \xi$
III	$\delta_3 < \delta < \delta_2$	R_1	$0 < \xi < \xi_2$
		R_2	$\xi_2 < \xi$
IV	$\delta_4 < \delta < \delta_3$	R_1	$\xi < \xi_2$
		R_3	$\xi_2 < \xi < \xi_3$
		R_2	$\xi_3 < \xi$
V	$0 < \delta < \delta_4$	R_1	$\xi < \xi_2$
		R_3	$\xi_2 < \xi < \xi_{max} = 1 - \cos\dfrac{\pi}{N_1}$

The resolution function as determined by computer simulation is depicted in Figs. 9 (for various values of δ or q, respectively) and 10 (with d/r as parameter, for a q far from a resonance, domain I). Figure A3 is the simulation equivalent of $\xi_{max}(\delta)$ of the schematic Fig. A2. Almost the whole length of the curve $\xi_{max}(\delta)$ is of the partial-overlap type. Full overlap gives $\xi_{max} = 1 - \cos \pi/3$ for $\delta < \delta_4 = 0.0004$ and no overlap occurs for $\delta > \delta_1 = 0.024$. Practically the best resolution is already attained for $\delta > \delta_2 = 0.009$.
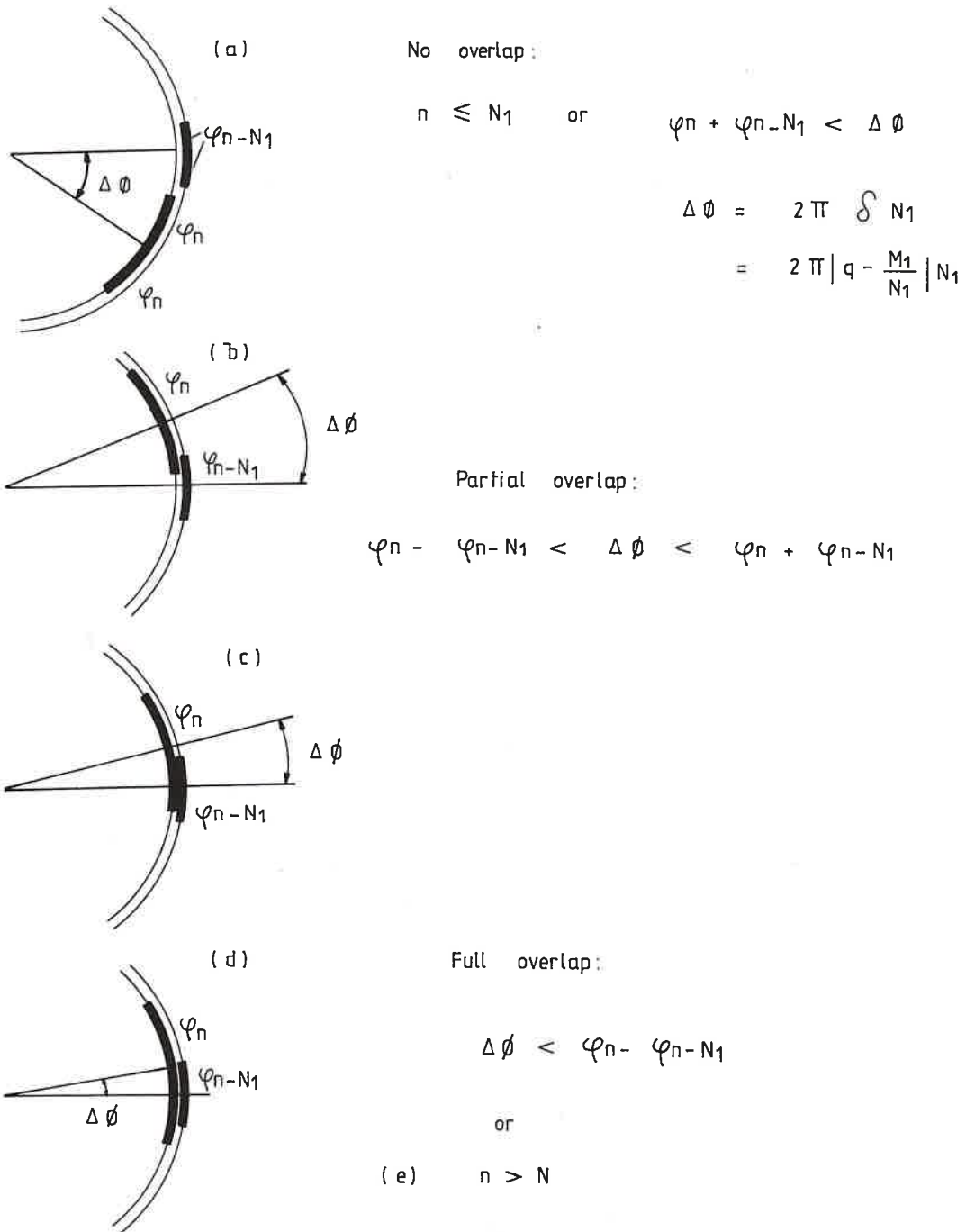
(a)

No overlap :

$$n \leq N_1 \quad \text{or} \quad \varphi_n + \varphi_{n-N_1} < \Delta \emptyset$$

$$\Delta \emptyset = 2\pi \, \delta \, N_1$$

$$= 2\pi \left| q - \frac{M_1}{N_1} \right| N_1$$

(b)

Partial overlap :

$$\varphi_n - \varphi_{n-N_1} < \Delta \emptyset < \varphi_n + \varphi_{n-N_1}$$

(c)

(d)

Full overlap :

$$\Delta \emptyset < \varphi_n - \varphi_{n-N_1}$$

or

(e) $\quad n > N$

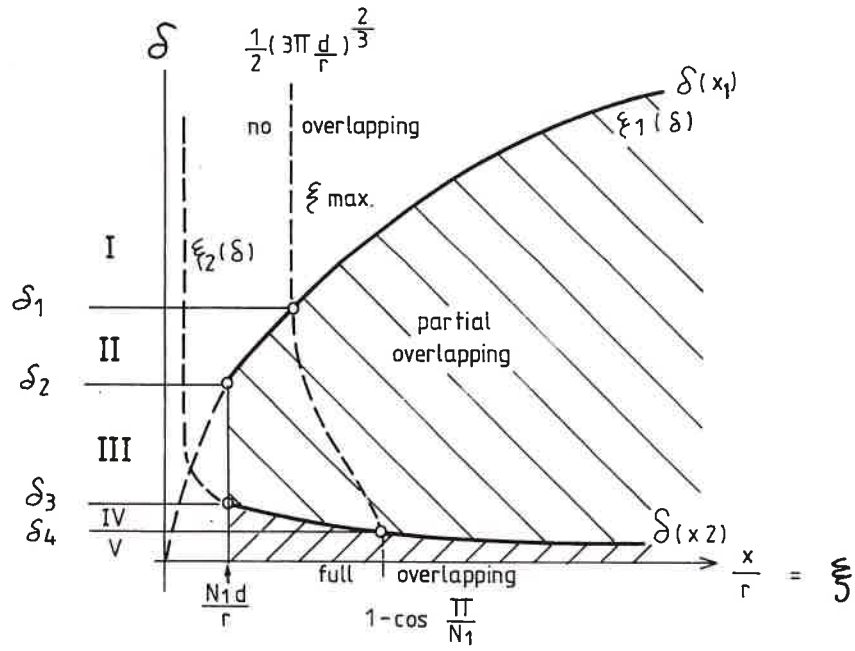Fig. A1 The different cases of overlapping cuts and their conditions.

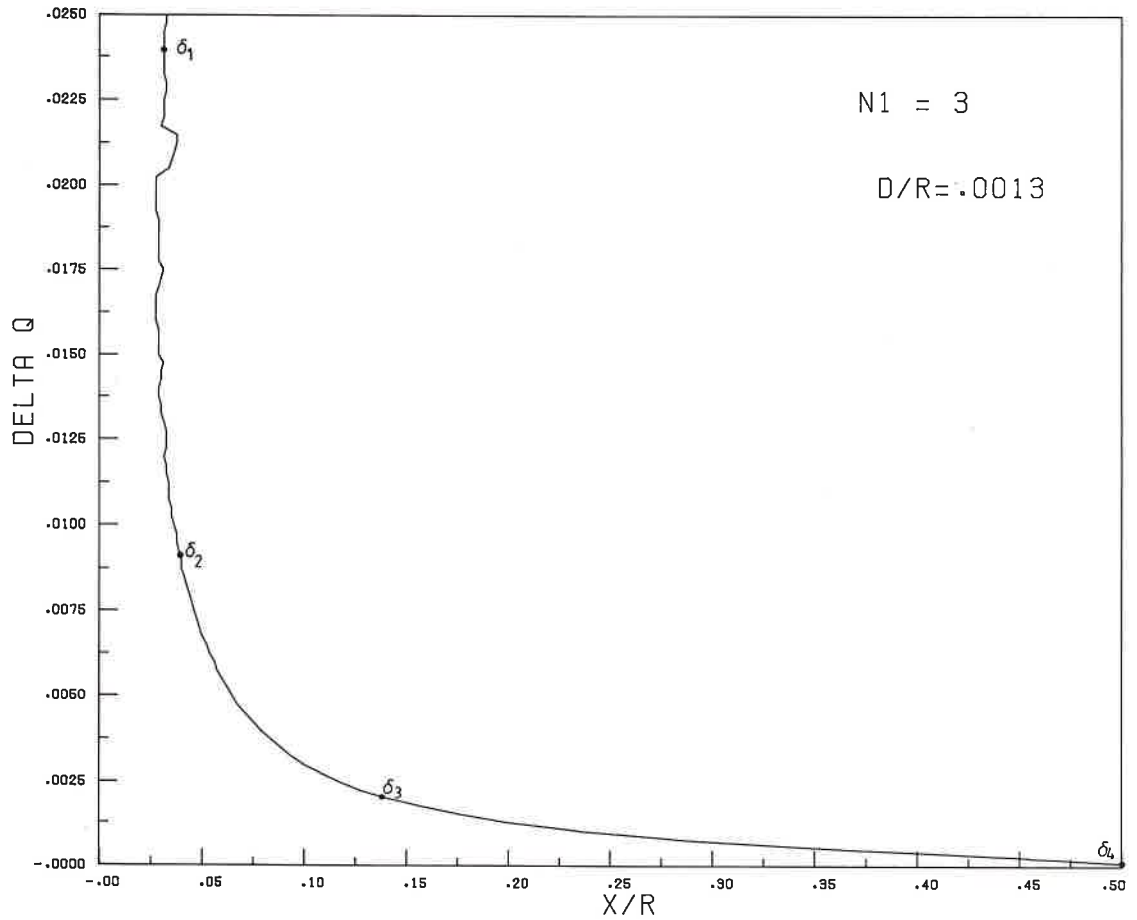**Fig. A2** Domains of different types of overlap.

Fig. A3 Computer simulation of the curve $\xi_{max}(\delta)$ of Fig. A2 for realistic parameters.